Published in final edited form as:

Nature. 2018 August ; 560(7717): 185–191. doi:10.1038/s41586-018-0368-8.

Functional aspects of meningeal lymphatics in aging and Alzheimer's disease

Sandro Da Mesquita[1,2,‡,#], **Antoine Louveau**[1,2,‡], **Andrea Vaccari**[3], **Igor Smirnov**[1,2], **R. Chase Cornelison**[4], **Kathryn M. Kingsmore**[4], **Christian Contarino**[1,2,5], **Suna Onengut-Gumuscu**[6], **Emily Farber**[6], **Daniel Raper**[1,2,7], **Kenneth E. Viar**[1,2], **Romie D. Powell**[1,2], **Wendy Baker**[1,2], **Nisha Dabhi**[1,2], **Robin Bai**[1,2], **Rui Cao**[4], **Song Hu**[4], **Stephen S. Rich**[6], **Jennifer M. Munson**[4,8], **M. Beatriz Lopes**[9], **Christopher C. Overall**[1,2], **Scott T. Acton**[3], and **Jonathan Kipnis**[1,2,#]

[1]Center for Brain Immunology and Glia (BIG), University of Virginia, Charlottesville, VA 22908, USA

[2]Department of Neuroscience, University of Virginia, Charlottesville, VA 22908, USA

[3]Virginia Image and Video Analysis Laboratory, Department of Electrical & Computer Engineering and Department of Biomedical Engineering, University of Virginia, Charlottesville, VA 22904, USA

[4]Department of Biomedical Engineering, University of Virginia, Charlottesville, VA 22908, USA

[5]Department of Mathematics, University of Trento, Povo, TN 38123, Italy

[6]Center for Public Health Genomics, University of Virginia, Charlottesville, VA 22908, USA

[7]Department of Neurosurgery, University of Virginia Health System, Charlottesville, VA 22908, USA

[8]Department of Biomedical Engineering & Mechanics, College of Engineering, Virginia Tech, Blacksburg, VA, 24061

[9]Department of Pathology, University of Virginia, Charlottesville, VA 22908, USA

[#]Correspondence: S.D.M. (sd8tf@virginia.edu) or J.K. (kipnis@virginia.edu); Tel: 001 434-983 3858/9, Fax: 001 434-982-4380.
[‡]Equal contribution

Correspondence and requests for materials should be addressed to S.D.M. (sd8tf@virginia.edu) and J.K. (kipnis@virginia.edu).

Author Contributions. S.D.M. designed and performed the experiments, analyzed and interpreted the data and wrote the manuscript; A.L. designed and performed the experiments and participated in manuscript preparation; A.V. developed the software (Lymph4D) for MRI data processing and analysis; I.S. surgeries and behavior testing; C.C. T2-weighted MRI, MRA and MRV acquisition and data analysis; R.C.C. hydrogels for transcranial peptide delivery; K.M.K. brain T1-weighted MRI acquisition; S.O.G. and E.F. RNA-seq experiments; D.R., K.E.V., R.D.P., W.B., N.D. and R.B. assisted with experimental procedures; R.C. and S.H. Photoacoustic imaging; S.S.R. and J.M.M provided resources and were involved in experimental design; M.B.L. human tissue samples; C.C.O. RNA-seq raw data analysis, data interpretation and manuscript writing; S.T.A. participated in the development of a software (Lymph4D), provided resources and intellectual contributions; J.K. designed the experiments, provided intellectual contribution, oversaw data analysis and interpretation and wrote the manuscript.

Competing interests: Jonathan Kipnis is an Advisor to PureTech Health/Ariya

Extended data is linked to the online version of the paper at www.nature.com/nature.

Supplementary information is linked to the online version of the paper at www.nature.com/nature.

Abstract

Aging is a major risk factor for many neurological pathologies and the mechanisms underlying brain aging remain elusive. Unlike other tissues, the central nervous system (CNS) parenchyma is devoid of lymphatic vasculature and removal of waste products is performed mainly through a paravascular route. (Re)discovery and characterization of meningeal lymphatic vessels prompted for an assessment of their role in CNS waste clearance. Here we show that meningeal lymphatics are draining macromolecules from the CNS (CSF and ISF) into the cervical lymph nodes. Impairment of meningeal lymphatic function slows paravascular influx of CSF macromolecules and efflux of ISF macromolecules, and induces cognitive impairment. Treatment of aged mice with vascular endothelial growth factor C enhances meningeal lymphatic drainage of CSF macromolecules, improving brain perfusion and learning and memory performance. Disruption of meningeal lymphatic vessels in transgenic mouse models of Alzheimer's disease (AD) promotes amyloid deposition in the meninges, which closely resembles human meningeal pathology, and aggravates parenchymal amyloid accumulation. Our findings suggest that meningeal lymphatic dysfunction may be an aggravating factor in AD pathology and in age-associated cognitive decline. Thus, augmentation of meningeal lymphatic function might be a promising therapeutic target for preventing or delaying age-associated neurological diseases.

The CNS has been for decades referred as an immune privileged organ[1], due to its limited interaction with the immune system, especially under homeostatic healthy conditions[2,3]. Although immune cells do not enter the parenchyma of the healthy brain, their surveillance of the CNS takes place within the meningeal spaces, where a great variety of immune cells is found[2,3]. Our group along with others[4,5], have recently (re)discovered and characterized the lymphatic vessels within the meninges (of rodents[4], non-human primates and humans[6]), although the role of these vessels in CNS function and in pathologies remains elusive.

Body tissues are perfused by interstitial fluid (ISF), which is locally reabsorbed via the lymphatic vascular network. In contrast, the parenchyma of the CNS is devoid of lymphatic vasculature[2]; in the brain, removal of cellular debris and toxic molecules, such as amyloid beta (Aβ) peptides, is mediated by a combination of transcellular transport mechanisms across the blood−brain and blood−cerebrospinal fluid (CSF) barriers[7–9], phagocytosis and digestion by resident microglia and recruited monocytes/macrophages[10,11], and CSF influx and ISF efflux through a paravascular (glymphatic) route[12–14]. The (re)discovery and characterization of meningeal lymphatic vessels prompted for a reassessment of the pathways of CNS waste clearance[4,5]. The role of this vasculature in brain function, specifically in the context of aging and AD, has not been studied. AD is the most common form of dementia and its prevalence increases with age[15,16]. Extracellular deposition of Aβ aggregates, the main constituent of senile plaques, is considered a pathological hallmark of AD that contributes to neuronal dysfunction and behavioral changes[16,17]. It is interesting to note that Aβ protein was initially isolated from homogenates of meningeal tissue from AD patients[18]. However, the mechanisms underlying the accumulation of Aβ in the AD brain and meninges are still not fully understood. Aging-associated decrease of paravascular recirculation of CSF/ISF[13] is thought to be responsible, at least in part, for the accumulation of Aβ in the brain parenchyma[12,13,19]. Aging also leads to progressive lymphatic vessel dysfunction in peripheral tissues[20–22]. However, little is known about a possible functional

decay of the CSF-draining meningeal lymphatics with age and how this might influence CNS amyloid pathology in AD.

Here we show that meningeal lymphatic vessels play an essential role in maintaining brain homeostasis by draining macromolecules from the CNS (CSF and ISF) into the cervical lymph nodes. Using pharmacological, surgical, and genetic models we show that impairment or enhancement of meningeal lymphatic function in mice affects paravascular influx of CSF macromolecules, efflux of ISF macromolecules and cognitive task performance. Our findings demonstrate that meningeal lymphatic vessel dysfunction may be one of the underlying factors for worsened amyloid pathology and cognitive deficits in AD and might be therapeutically targeted to alleviate age-associated cognitive decline.

Meningeal lymphatics and brain perfusion

Given the close communication and ongoing exchange of molecular contents between the CSF and ISF[5,12], we postulated that brain influx of CSF macromolecules through the paravascular pathway is impacted by the meningeal lymphatics. To test this hypothesis, we ablated meningeal lymphatic vessels by injecting a photodynamic drug, Visudyne (verteporfin for injection), into the CSF, which upon photoconversion has been shown to preferentially damage the lymphatic endothelial cells (LECs)[23,24]. Injection of vehicle followed by photoconversion and of Visudyne without the photoconversion step were used as two controls (Fig. 1a). The use of this method resulted in effective ablation of meningeal lymphatics lasting for at least 7 days (Fig. 1b, c), without any detectable off-target effect in meningeal blood vasculature coverage (Fig. 1d). To confirm functional impairment upon meningeal lymphatic ablation, we injected 5 μL of fluorescent ovalbumin-Alexa 647 (OVA-A647; ~45 kDa) into the cisterna magna (i.c.m.) and measured the drainage of this tracer from the CSF into the deep cervical lymph nodes (dCLNs) (Extended data Fig. 1a). A significant reduction in OVA-A647 drainage was observed in the Visudyne/photoconversion group compared to controls (Extended data Fig. 1b). Importantly, the structure of major intracranial veins and arteries was not altered (Extended data Fig. 1c–h). Likewise, the integrity of the blood-brain barrier, assessed by T1-weighted magnetic resonance imaging (MRI) after intravenous injection of gadolinium (Gd) as contrast agent (Extended data Fig. 1i, j), or the ventricular volume measured by T2-weighted SPACE MRI (Extended data Fig. 1k–m) also remained unaltered after ablation of meningeal lymphatics.

To avoid any confounding effects of increased intracranial pressure (ICP) after i.c.m. injection, we measured changes in ICP after injecting different volumes of OVA-A647 (Extended data Fig. 2a, b). There was a transient increase in ICP during i.c.m. injection of tracer, followed by a drop in ICP upon post-injection removal of the syringe (Extended data Fig. 2a). Mice injected with 2 μL presented ICP values lower than baseline even 120 min post-injection (Extended data Fig. 2b). However, a significant decrease in drainage to the dCLNs was equally observed in lymphatic ablated mice upon injection of 2 μL (Extended data Fig. 2c–e) or 5 μL of tracer (Extended data Fig. 1a, b), when compared to controls.

Brain perfusion by the CSF tracer was found to be significantly lower in the Visudyne/photoconversion group than in their control counterparts (Fig. 1e, f and Extended data Fig.

2f, g). Similar findings on brain perfusion by CSF were observed when meningeal lymphatic drainage was disrupted by surgical ligation of the vessels afferent to the dCLNs (Extended data Fig. 3a–d). Prospero homeobox protein 1 (Prox1) heterozygous mice, a genetic model of lymphatic vessel malfunction[25], also presented impaired perfusion through the brain parenchyma and impaired CSF drainage (Extended data Fig. 3e–i). Altogether, three different models of impaired meningeal lymphatic function (pharmacological, surgical, and genetic) showed a significant impact on brain perfusion by CSF macromolecules.

To evaluate the effect of meningeal lymphatic ablation on the rate of brain perfusion by CSF, we injected Gd (i.c.m.) and performed brain T1-weighted MRI. Three different concentrations of Gd—1, 10 and 25 mM—were tested (Extended data Fig. 3j, k) and, due to better signal-to-noise ratio, the 25 mM concentration was used in subsequent experiments (Fig. 1g). A software developed in-house, Lymph4D (see Supplementary Methods section for more details), was used to process and analyze the images acquired by MRI. After 16 sequences of MRI acquisition (~52 min), the observed signal gain in two brain regions (hippocampus and cortex) was significantly lower in the Visudyne group when compared to vehicle-treated (Fig. 1h, i and Extended data Fig. 3l, m). Interestingly, along with the lower influx of Gd into the parenchyma, we observed higher contrast in signal intensity (over ~52 min) in the ventricles of Visudyne-treated mice, suggesting Gd accumulation in the CSF (Extended data Fig. 3n). Whether this observation is concomitant with ventricular CSF reflux (a phenomenon reported in patients with idiopathic normal pressure hydrocephalus[26]) warrants further investigation. Moreover, using the advection-diffusion model in Lymph4D, we found that mice presented lower coefficient values of isotropic diffusion of Gd in the brain after meningeal lymphatic ablation (Extended data Fig. 3o, p), suggesting a lower rate of molecular diffusion in the brain parenchyma when meningeal lymphatic drainage is reduced.

Within the brain parenchyma, it was shown that astrocytes play an important role in the modulation of paravascular CSF macromolecule influx and efflux (glymphatic[12]) through aquaporin 4 (AQP4)[12,13]. Deletion of *Aqp4* in AD transgenic mice also resulted in increased amyloid plaque burden and exacerbated cognitive impairment[19]. Moreover, decreased perivascular AQP4 localization was observed in brain tissue from AD patients[27]. We could not detect changes either in overall brain coverage by AQP4 (Extended data Fig. 3q, r) or in perivascular localization of $AQP4^+$ astrocytic endfeet between vehicle-treated and Visudyne-treated mice (Extended data Fig. 3s–v), suggesting that upon meningeal lymphatic dysfunction, impairment of brain perfusion by CSF is independent of AQP4.

Next, we examined whether the efflux of ISF macromolecules from the brain parenchyma would also be affected by meningeal lymphatics. We used three different tracers, the smaller peptides $A\beta_{42}$-HyLite647 (~4 kDa) and OVA-A647, and the large protein complex, low density lipoprotein-BODIPY FL (LDL-BODIPY FL, ~500 kDa). One hour after stereotaxic injection, the levels of the remaining tracers were assessed in the parenchyma of mice from lymphatic ablated or control groups (Extended data Fig. 4a–h). Independently of the nature of the fluorescent tracer, higher levels of remnants were detected in the brains of mice from the Visudyne/photoconversion groups when compared to both control groups (Extended data Fig. 4a–h). These findings, as suggested before[5], demonstrate that efflux of

parenchymal/ISF macromolecules and their drainage into dCLNs are impaired as a consequence of meningeal lymphatic dysfunction, therefore functionally connecting meningeal lymphatics with CSF influx/ISF efflux mechanisms.

To understand the implications of impaired meningeal lymphatics for brain function, we performed meningeal lymphatic ablation twice, allowing a two-week interval between procedures to ensure prolonged lymphatic ablation, and then assessed mice behavior in the open field (OF), novel location recognition (NLR), contextual fear conditioning (CFC), and Morris water maze (MWM) tests (Fig. 1j). No differences between the groups were detected in total distance and time spent in the center of the arena in the open field test (Extended data Fig. 5a, b) or in time spent with the object placed in a novel location in the NLR test (Extended data Fig. 5c, d). A significant difference between control groups and Visudyne/photoconversion group was observed in the cued test of the CFC (Extended data Fig. 5e, f), which points to an impairment in fear memory and in hippocampal-amygdala neuronal circuitry[28] in mice with impaired meningeal lymphatic function. Mice with ablated meningeal lymphatics also showed significant deficits in spatial learning in the MWM (Fig. 1k–o). Similar impairments in spatial learning and memory were observed in mice that had undergone lymphatic ligation (Extended data Fig. 5g–j), supporting the notion that the observed effect is a result of dysfunctional meningeal lymphatic drainage and not an artifact of the ablation method using Visudyne.

Using RNA sequencing (RNA-seq) we assessed the effect of Visudyne/photoconversion treatment on hippocampal gene expression before and after performing MWM. Principal component analysis showed that four weeks of meningeal lymphatic ablation did not induce significant changes in the hippocampal transcriptome (Extended data Fig. 5k, l). However, significant differences in hippocampal gene expression were unfolded in response to MWM performance after prolonged meningeal lymphatic ablation (Extended data Fig. 5m, n). Contrary to what was observed without MWM performance (Extended data Fig. 5k, l), individual samples from each group clustered together after the mice performed the test (Extended data Fig. 5m, n). Interestingly, although the fold change of significantly altered genes after lymphatic ablation and MWM was moderate ($-1.79 < \log2(\text{fold change}) < 1.69$), functional enrichment analysis (Extended data Fig. 5o, p) revealed changes in gene sets associated with neurodegenerative diseases, such as Huntington’s, Parkinson’s and Alzheimer’s (Extended data Fig. 5o). Significant transcriptional alterations were also associated with excitatory synaptic remodeling and plasticity, hippocampal neuronal transmission[29], learning and memory and aging-related cognitive decline[30] (Extended data Fig. 5q, r). Furthermore, different gene sets involved in the regulation of metabolite generation and processing, glycolysis and mitochondrial respiration and oxidative stress were also significantly altered in the hippocampus upon lymphatic ablation and performance of the behavior test (Extended data Fig. 5p, s–v).

Meningeal lymphatics in aging

Aging is the principal risk factor for many neurological disorders, including AD[15,16], and has a detrimental effect on brain CSF/ISF paravascular recirculation[13]. The reported findings that aging is also associated with peripheral lymphatic dysfunction[20–22] led us to

hypothesize that deterioration of meningeal lymphatic vessels underlies some aspects of age-associated cognitive decline. Indeed, and in agreement with a previous study[13], old mice demonstrate reduced brain perfusion by CSF macromolecules as compared to young counterparts (Extended data Fig. 6a, b). Impaired brain perfusion by CSF in old mice was accompanied by a decrease in meningeal lymphatic vessel diameter and coverage, as well as decreased drainage of CSF macromolecules into dCLNs in both females and males (Extended data Fig. 6c–f). To further address the effect of aging on meningeal lymphatics, we performed RNA-seq analysis of LECs sorted from the meninges of young-adult and old mice (Extended data Fig. 6g and Fig. 2a). Differential expression of 607 genes was detected in the meningeal LECs of old when compared to young-adult mice (Fig. 2a). Of note, the expression of genes encoding for classical markers of LECs, including *Flt4* that encodes the vascular endothelial growth factor C (VEGF-C) receptor tyrosine kinase VEGFR3, was not significantly altered at 20–24 months (Fig. 2b). Enrichment analysis revealed, however, changes in gene sets involved in immune and inflammatory responses, phospholipid metabolism, extracellular matrix organization, cellular adhesion and endothelial tube morphogenesis, all suggestive of functional alterations in meningeal LECs with age (Fig. 2c). The altered expression of genes involved in transmembrane receptor protein tyrosine kinase signaling pathway in old mice, namely the down-regulation of *Cdk5r1*[31], *Adamts3*[32] and *Fgfr3*[33], pointed to possible changes in signaling by lymphangiogenic growth factors in old meningeal LECs (Fig. 2d).

We have previously shown that treatment with recombinant VEGF-C increases the diameter of meningeal lymphatic vessels[4]. Furthermore, delivery of VEGF-C by adenoviral gene therapy was previously found to efficiently boost peripheral lymphatic sprouting and function[34,35]. A similar adeno-associated virus serotype 1 (AAV1) vector was used here to express mVEGF-C or enhanced green fluorescent protein (EGFP) as control. At 2 and 4 weeks post i.c.m. injection, AAV1-infected cells expressing EGFP were limited to the pia around the brain, meninges (dura and arachnoid), and pineal gland (Extended data Fig. 6h–j). Treatment of young mice with AAV1-CMV-mVEGF-C resulted in a significant increase in meningeal lymphatic vessel diameter, without affecting blood vessel coverage (Extended data Fig. 6k–m).

Treatment of old mice (at 20–24 months) with AAV1-CMV-mVEGF-C also resulted in increased lymphatic vessel diameter (as compared to AAV1-CMV-EGFP) without detectable off-target effects on the meningeal blood vasculature coverage and on meningeal/brain vascular hemodynamics (Fig. 2e–h and Extended data Fig. 6n–p). One month after AAV1-CMV-mVEGF-C treatment, old mice showed a significant increase in CSF tracer drainage into the dCLNs, which was not due to increased lymphatic vessel coverage in the nodes (Fig. 2i, j). Importantly, the rate of tracer influx into the brain parenchyma was significantly increased as a result of enhanced meningeal lymphatic function (Fig. 2k, l and Extended data Fig. 6q, r).

Transcranial delivery (through a thinned skull surface) of hydrogel-encapsulated VEGF-C peptide also resulted in increased diameter of meningeal lymphatics in young and old mice (Extended data Fig. 7a–c). This VEGF-C treatment led to a significant increase in the function of meningeal lymphatics in old mice, whereas young-adult mice did not respond to

the treatment (Extended data Fig. 7d, e), probably due to the ceiling effect of their existing drainage capacity. The increased drainage after VEGF-C treatment in old mice also correlated with enhanced brain perfusion by CSF macromolecules (Extended data Fig. 7f, g).

To avoid potential VEGF-C off-target effects on the blood vasculature through VEGFR2[34,36], we employed transcranial delivery of VEGF-C156S (Extended data Fig. 7h), a mutant protein that binds specifically to VEGFR3 and spares its effects on VEGFR2[34,36]. Treatment with VEGF-C156S resulted in a significant increase in meningeal lymphatic diameter (Extended data Fig. 7i, j), drainage of tracer from the CSF (Extended data Fig. 7k, l), and paravascular influx of tracer into the brains of old mice (Extended data Fig. 7m, n).

To determine the functional role of enhanced meningeal lymphatics in the learning behavior of mice at different ages we again used viral delivery of mVEGF-C (Extended data Fig. 7o–u). This method was selected to avoid submitting aged mice to consecutive surgeries, involving general anesthesia and skull thinning. Treatment of young-adult mice with AAV1-CMV-mVEGF-C for 1 month did not improve spatial learning and memory (Extended data Fig. 7p, s), suggestive of a ceiling effect in MWM performance at this age. However, AAV1-CMV-mVEGF-C treatment resulted in significant improvement in the latency to platform and in the percentage of allocentric navigation strategies, in the MWM reversal in 12–14 months-old mice (Extended data Fig. 7q, t) and in the MWM acquisition and reversal in 20–22 months-old mice (Extended data Fig. 7r, u), when compared to AAV1-CMV-EGFP-treated age-matched mice.

Increased expression of VEGF-C in the adult brain has been previously shown to boost hippocampal neural stem cell proliferation[37]. Although spatial learning and memory in the MWM is not dependent on adult hippocampal neurogenesis[38], we examined the number of Ki67 expressing cells in the hippocampal dentate gyrus of mice treated with EGFP or mVEGF-C viral vectors at 3, 12–14 and 20–22 months of age. No differences in cell proliferation in the dentate gyrus were observed after mVEGF-C treatment (Extended data Fig. 7v, w).

To demonstrate that the beneficial effect of mVEGF-C treatment on cognitive behavior was through improved meningeal lymphatic drainage, we injected old mice with the EGFP or mVEGF-C viruses and concomitantly ligated the lymphatics afferent to the dCLNs. Assessment of learning and memory was performed 1 month after the procedures (Fig. 2m). The beneficial effect of mVEGF-C treatment in mice from the sham group, which performed significantly better in the NLR (Fig. 2n, o) and in the MWM (Fig. 2p–r) tests, was abrogated in mice submitted to ligation of the CSF-draining lymphatics. Accordingly, the drainage of CSF macromolecules into dCLNs was significantly higher in the sham-operated mice treated with mVEGF-C when compared to all other groups (Fig. 2s, t).

Dysfunctional lymphatics in amyloid pathology

Based on previous findings concerning the role of paravascular CSF/ISF recirculation in the context of AD[12,14,19,27] and our present results on the interdependence between meningeal

lymphatic function and brain perfusion by CSF, we postulated that modulating meningeal lymphatic function would impact the behavior and brain pathology in AD transgenic mice. The potential effect of mVEGF-C treatment (through viral vector delivery) was first tested on J20 transgenic mice at 6–7 months of age (Extended data Fig. 8a–n), when mice already present marked cognitive deficits and start to show amyloid deposition in the brain parenchyma[39,40]. We were not able to improve J20 mice hyperactive phenotype in the open field or cognitive performance in the MWM (Extended data Fig. 8a–f). Moreover, viral expression of mVEGF-C did not significantly affect meningeal lymphatic vessel diameter, the level of Aβ in the CSF, or amyloid deposition in the hippocampus (Extended data Fig. 8g–n). In order to explain the lack of effect of the mVEGF-C treatment in J20 mice, we measured meningeal lymphatic drainage in J20 mice and in wild-type (WT) littermate controls. The same measurement was performed in a more aggressive AD transgenic mouse model—the 5xFAD—that already presents amyloid plaques at 3 months of age[41] (Extended data Fig. 8o). Independently of the model, the level of CSF tracer drained into the dCLNs was comparable between AD transgenic mice and age-matched WT littermates (Extended data Fig. 8p–s). Similarly, meningeal lymphatic vessel morphology and coverage did not differ between WT and 5xFAD mice at 3–4 months of age (Extended data Fig. 8t, u). Collectively, these data point to no apparent meningeal lymphatic dysfunction in AD transgenic mice at younger ages, which might explain the inefficacy of mVEGF-C treatment.

Although age is the major risk factor for late-onset AD[15,16], most transgenic mouse models that mimic early-onset AD develop amyloid pathology at young age and, therefore, may be lacking the aspect of age-related lymphatic dysfunction. To this end, we induced prolonged meningeal lymphatic ablation in 5xFAD mice by repeated (every 3 weeks) injection and photoconversion of Visudyne for a total of 1.5 months, starting at ~2 months of age (Fig. 3a). Taking into account the marked brain amyloid deposition presented by these mice at ~3 months of age, surprisingly, no obvious Aβ deposition was detected in the meninges of 5xFAD mice from the two control groups (Fig. 3b). Yet, the 5xFAD mice with ablated meningeal lymphatics demonstrated marked deposition of amyloid in the meninges (Fig. 3b), as well as macrophage recruitment to large Aβ aggregates (Fig. 3c). Photoacoustic imaging 1 week after lymphatic ablation demonstrated no differences in blood flow and oxygenation between 5xFAD mice from the different groups (Extended data Fig. 9a–c). Assessment of lymphoid and myeloid cell populations in the meninges (Extended data Fig. 9d) demonstrated a significant increase in the number of macrophages upon lymphatic ablation, when compared to both control groups (Extended data Fig. 9e), which might be correlated with increased amyloid deposition and inflammation in the meninges. Interestingly, along with meningeal amyloid pathology, we observed an aggravation of brain amyloid burden in the hippocampi of 5xFAD mice with dysfunctional meningeal lymphatics (Fig. 3d–g). A similar outcome was observed in J20 transgenic mice after a total of 3 months of meningeal lymphatic ablation (Extended data Fig. 9f); Aβ aggregates had formed in the meninges (Extended data Fig. 9g) and the Aβ plaque load in the hippocampi was significantly increased (Extended data Fig. 9h–k).

The observed meningeal amyloid pathology in mice after meningeal lymphatic vessel ablation led us to assess meningeal amyloid pathology in AD patients (Fig. 3h). Staining for Aβ in the brains of 9 AD patients and 8 non-AD controls (Extended data Table 1) revealed,

as expected, marked parenchymal deposition of amyloid in the AD, but not in the non-AD brains (Extended data Fig. 9l, m). Interestingly, when compared to tissue from non-AD cases, all samples from AD patients demonstrated striking vascular amyloid pathology in the cortical leptomeninges (Extended data Fig. 9l, m) and Aβ deposition in the dura mater adjacent to the superior sagittal sinus (Fig. 3i, j) or further away from the sinus (Fig. 3k, l). Macrophages in the dura of AD cases were also found in close proximity to Aβ deposits (Fig. 3l). These findings showed that prominent meningeal amyloid deposition observed in AD patients is also observed in AD mouse models after meningeal lymphatic vessel ablation.

Discussion

Altogether, the present findings highlight the importance of meningeal lymphatic drainage in brain physiology. Meningeal lymphatic dysfunction in young-adult mice results in impaired brain perfusion by CSF and in learning and memory deficits. Aged mice demonstrated significant disruption of meningeal lymphatic function, which may underlie some of the aspects of age-associated cognitive decline. Augmentation of meningeal lymphatic drainage in aged mice can ultimately facilitate the clearance of CSF/ISF macromolecules from the brain, resulting in improved cognitive function. We also show that transgenic AD mouse models recapitulate many features of brain amyloid pathology observed in AD patients, but not the deposition of amyloid observed in the dura mater. However, inducing meningeal lymphatic dysfunction in mouse models of AD worsened amyloid pathology in the meninges and in the brain. It would be interesting to see if AD transgenic mice, particularly the ones with a less aggressive phenotype, when sufficiently aged, would exhibit meningeal amyloid pathology. Furthermore, taking into account the role of the brain vascular endothelium and of other components of the blood-brain barrier, such as pericytes, in the excretion of Aβ from the brain[7–9,42], it would be very interesting to explore a possible connection between age-associated meningeal lymphatic dysfunction, impaired CSF/ISF recirculation, and decreased fitness of the blood-brain barrier and its cellular components.

Finally, it is vital to determine whether aging-related changes in meningeal lymphatic drainage might affect the efficacy of current therapies for AD, such as antibody-based treatments[43]. Modulation of meningeal lymphatic function in aged individuals might represent a novel preventive therapeutic strategy, not only to delay AD initiation and progression but also for use against other brain proteinopathies that are exacerbated by aging.

METHODS

Mouse strains and housing

Male or female wild-type mice (C57BL/6J background) were either bred in-house, purchased from the Jackson Laboratory (Bar Harbor, Maine, USA) or provided by the National Institutes of Health/National Institute on Aging (Bethesda, MD, USA). All mice were maintained in the animal facility for habituation for at least 1 week prior to the start of the manipulation/experimentation. C57BL/6J wild-type mice were tested at 2–3, 12–14 and 20–24 months of age. Male hemizygous B6.Cg-Tg(*PDGFB-APPSwInd*)20Lms/2Mmjax

(J20, JAX stock #006293) and B6.Cg-Tg(*APPSwFlLon,PSEN1*M146L*L286V*)6799Vas/Mmjax (5xFAD, JAX stock #008730) were purchased from the Jackson Laboratory and bred in-house on a C57BL/6J background. J20 hemizygous mice present diffuse Aβ deposition in the dentate gyrus and neocortex at 5–7 months, with all transgenic mice exhibiting plaques by the age of 8–10 months[44]. 5xFAD hemizygous mice overexpress the transgene constructs under neural-specific elements of the mouse thymocyte differentiation antigen 1 promoter and present accelerated accumulation of $A\beta_{42}$ and deposition of amyloid and gliosis in the brain starting at 2 months of age, with dramatic amyloid plaque load without major behavioral deficits at 5 months[45]. In-house bred male transgene carriers and non-carrier (WT) littermates were used at different ages that are indicated throughout the manuscript. $Prox1^{LacZ}$ mice (designated $Prox1^{+/-}$ mice in this manuscript) on a NMRI background (kindly provided by Dr. Guillermo Oliver, Northwestern University, Chicago, IL) were also bred in-house and used in this study as a constitutive model for dysfunctional lymphatic vessels[46]. Mice of all strains were housed in an environment with controlled temperature and humidity, on 12 hours light/dark cycles (lights on at 7:00), and fed with regular rodent's chow and sterilized tap water *ad libitum*. All experiments were approved by the Institutional Animal Care and Use Committee of the University of Virginia.

Intra-cisterna magna injections

Mice were anaesthetized by intraperitoneal (i.p.) injection of a mixed solution of ketamine (100 mg/Kg) and xylazine (10 mg/Kg) in saline. The skin of the neck was shaved and cleaned with iodine and 70% ethanol, ophthalmic solution placed on the eyes to prevent drying and the mouse's head was secured in a stereotaxic frame. After making a skin incision, the muscle layers were retracted and the cisterna magna exposed. Using a Hamilton syringe (coupled to a 33-gauge needle), the volume of the desired tracer solution was injected into the CSF-filled cisterna magna compartment. For brain CSF influx and lymphatic drainage experiments, 2 or 5 μL of Alexa Fluor® 594 or 647 conjugated OVA (Thermo Fisher Scientific), at 0.5 mg/mL in artificial CSF (#597316, Harvard Apparatus U.K.), were injected at a rate of 2.5 μL/min. After injecting, the syringe was left in place for additional 2 min to prevent back-flow of CSF. The neck skin was then sutured, the mice were subcutaneously injected with ketoprofen (2 mg/Kg) and allowed to recover on a heating pad until fully awake. For details regarding changes in intracranial pressure associated with this injection methodology see the next section and Extended data Fig. 2.

Intracranial pressure measurement

Mice were anesthetized by i.p. injection with ketamine and xylazine in saline and the skin was incised to expose the skull. A 0.5 mm diameter hole was drilled in the skull above the right parietal lobe. Using a stereotaxic frame, a pressure sensor catheter (model SPR100, Millar) was inserted perpendicularly into the cortex at a depth of 1 mm. To record intracranial pressure (ICP) changes, the pressure sensor was connected to the PCU-2000 pressure control unit (Millar). For measurements of ICP while performing i.c.m. injections of 2 or 5 μL of tracer (following the same i.c.m. injection procedure as describe above), after stabilization of the signal (around a minute after insertion of the probe), average pressure was calculated over 1 min right before start injecting (pre-injection), over the last min of injection (during injection), over the last min of extra time used to prevent CSF back-flow

(post-injection with syringe in) and over the last 2 min of recording, specifically between minute 4 and 6 after taking out the syringe (post-injection with syringe out). For measurements in non-injected mice or in mice at different time-points (30, 60 and 120 min post-injection) after i.c.m. injection of 2, 5 or 10 μL of tracer, ICP was recorded for 6 min after stabilization of the signal and the average pressure was calculated over the last 2 minutes of recording (between minute 4 and 6 of the recording). All animals were euthanized at the conclusion of the measurement.

Meningeal lymphatic vessel ablation

Selective ablation of the meningeal lymphatic vessels was achieved by i.c.m. injection and transcranial photoconversion of Visudyne® (verteporfin for injection, Valeant Ophtalmics). Visudyne was reconstituted following manufacturer instructions and 5 μL was injected i.c.m. following the previously described procedure. After 15 min, an incision was performed in the skin to expose the skull bone and Visudyne was photoconverted by pointing a 689-nm wavelength non-thermal red light (Coherent Opal Photoactivator, Lumenis) on 5 different spots above the intact skull (1 on the injection site, 1 on the superior sagittal sinus, 1 at the junction of all sinuses and 2 on the transverse sinuses). Each spot was irradiated with a light dose of 50 J/cm^2 at an intensity of 600 mW/cm^2 for a total of 83 s. Controls were injected with the same volume of Visudyne (without the photoconversion step) or sterile saline plus photoconversion (vehicle/photoconversion). The scalp skin was then sutured, the mice were subcutaneously injected with ketoprofen (2 mg/Kg) and allowed to recover on a heating pad until fully awake.

Lymphatic vessel ligation

Surgical ligation of the lymphatics afferent to the dCLNs was performed as described before[47]. Briefly, mice were anaesthetized by i.p. injection with ketamine and xylazine in saline, the skin of the neck was shaved and cleaned with iodine and 70% ethanol and ophthalmic solution placed on the eyes to prevent drying. A midline incision was made 5 mm superior to the clavicle. The sternocleidomastoid muscles were retracted and the dCLNs were exposed on each side. Ligation of the afferent lymphatic vessels on each side was performed with 10-0 synthetic, non-absorbable suture. Control mice were submitted to a sham surgery consisting of the skin incision and retraction of the sternocleidomastoid muscle only. The skin was then sutured, the mice were subcutaneously injected with ketoprofen (2 mg/Kg) and allowed to recover on a heating pad until fully awake.

Brain parenchymal injections

Mice were anaesthetized by i.p. injection of ketamine and xylazine in saline and the head was secured in a stereotaxic frame. An incision was made in the skin to expose the skull and a hole was drilled at +1.5 mm in the anterior-posterior axis and −1.5 mm in the medial-lateral axis relative to bregma. Then, using a Hamilton syringe (coupled to a 33-gauge needle) placed at +2.5 mm in the dorsal-ventral axis (relative to bregma), 1 μL of either Alexa Fluor® 647 conjugated OVA (at 0.5 mg/mL), HiLyte™ Fluor 647 conjugated Aβ_{42} (at 0.05 μg/mL, AnaSpec, Inc.) or BODIPY™ FL conjugated low density lipoprotein (LDL) from human plasma (at 0.1 mg/mL, Thermo Fisher Scientific) in artificial CSF were injected at a rate of 0.2 μL/min into the brain parenchyma. Concentrations of the injected fluorescent

$A\beta_{42}$ and LDL molecular tracers were chosen in order to be comparable to levels detected in brain ISF of AD transgenic mice[47] and in plasma of C57BL/6 mice[48], respectively. After injecting, the syringe was left in place for additional 5 min to prevent back-flow. The scalp skin was then sutured, the mice were subcutaneously injected with ketoprofen (2 mg/Kg) and allowed to recover on a heating pad until further use.

AAV delivery

For experiments assessing the effect of viral-mediated expression of mVEGF-C (NM_009506.2) on meningeal lymphatics, 2 μL of artificial CSF containing 10^{13} genome copies per mL of AAV1-CMV-mVEGF-C, or control AAV1-CMV-EGFP (AAV1, adeno-associated virus serotype 1; CMV, cytomegalovirus promoter; EGFP, enhanced green fluorescent protein; purchased from Vector BioLabs, Philadelphia), were injected directly into the cisterna magna CSF at a rate of 2 μL/min, following the previously described i.c.m. injection procedure.

Transcranial recombinant VEGF-C delivery

A hydrogel of 1.4% hyaluronic acid and 3% methylcellulose alone (vehicle) or with 200 ng/mL of encapsulated human VEGF-C (PeproTech) or VEGF-C156S (R&D Systems) was prepared as described elsewhere[49]. Briefly, lyophilized, sterile methylcellulose (4000 cP, Sigma-Aldrich) and sterile hyaluronic acid (1500–1800 kDa, Sigma-Aldrich) were sequentially dissolved in sterile 0.1 M phosphate buffered saline (PBS) at 4 °C overnight. Lyophilized VEGF-C or VEGF-C156S were resuspended as particulate at 2000 ng/mL in 0.5% sterile methylcellulose in PBS. The particulate solution, or vehicle 0.5% methylcellulose, was mixed into the hydrogel pre-solution at 1:10, and loaded into a syringe for gelation at 37°C. The methylcellulose provided more stability, by promoting thermal gelation, and increased the hydrophobic properties of the gel[49], sustaining the release of VEGF-C or VEGF-C156S up to 7–10 days *in vitro* (verified using an ELISA for human VEGF-C, R&D Systems). The hydrogels were prepared on the day of the experiment and kept warm inside the individual syringes until applied onto the mouse's skull. The mouse was anaesthetized by i.p. injection of ketamine and xylazine in saline and the head was secured in a stereotaxic frame. An incision was made in the scalp skin and the skull was thinned at the junction of all sinuses and above the transverse sinus. The shear-thinning properties of the polymers allowed the extrusion of 100 μL of each hydrogel solution from the syringe into the thinned skull surface. The scalp skin was then sutured on top of the solidified hydrogel, the mice were subcutaneously injected with ketoprofen (2 mg/Kg) and allowed to recover on a heating pad until fully awake. Taking the into account the release kinetics of 7−10 days, hydrogels were re-applied, following the same methodology, 2 weeks after the first treatment.

MRI acquisitions and analysis

All MRI acquisitions were performed at the University of Virginia Molecular Imaging Core facilities in a 7T Clinscan system (Bruker, Ettlingen, Germany) equipped with a 30 mm diameter cylindrical RF Coil. Detailed description of MRI data acquisition, processing and analysis (including mathematical models and equations) can be found in the Supplementary information linked to the online version of the paper at www.nature.com/nature.

Photoacoustic imaging

Adult mice were maintained under anesthesia with 1.5% isoflurane and at a constant body temperature with the aid of a heating pad. A surgical incision was made in the scalp and the fascia was removed to expose the skull. One day prior to the imaging, the skull over the region of interest was thinned to the desired thickness (~100 μm). Mice were then imaged by multi-parametric photoacoustic microscopy, which is capable of simultaneously image oxygen saturation of hemoglobin (sO2) and blood flow speed as described previously[50]. Using the oxy-hemoglobin and deoxy-hemoglobin values, recorded using two nanosecond-pulsed lasers (532 and 559 nm), it is possible to compute the final sO2. Correlation analysis of adjacent A-line signals allows the quantification of blood flow speed within individual vessels. By segmenting major vessels within the region of interest, average values of the blood flow speed and sO2 were extracted for quantitative analysis.

Open field test

Open field was performed following a published protocol[51] with minor modifications. Mice were carried to the behavior room to habituate at least 30 min before starting the test. Mice were then placed into the open field arena (made of opaque white plastic material, 35 cm × 35 cm) by a blinded experimenter and allowed to explore it for 15 min. Total distance (cm) and % time spent in the center (22 cm × 22 cm) were quantified using video tracking software (TopScan, CleverSys, Inc.).

Novel location recognition test

Novel location recognition test was performed following a published protocol[52] with modifications. The experimental apparatus used in this study was the same square box made of opaque white plastic (35 cm × 35 cm) used in the Open field test. The mice were first habituated to the apparatus for 15 min. Two different plastic objects (one red and the other blue and with different shapes) were then positioned in a defined spatial orientation, namely on each corner of the arena and 5 cm away from each adjacent arena wall. Mice were then placed in the arena (by a blinded experimenter), facing the wall farther away from the objects and allowed to explore the arena and objects for 10 min. Twenty-four hours later, the mice were placed in the same box with the same two objects, but one of them had switched location and was placed in a new quadrant, obliquely to the familiar object (novel location test). The time spent exploring the objects in the familiar and novel locations was also measured for 10 min. Exploration of an object was assumed when the mouse approached an object and touched it with its vibrissae, snout or forepaws and was measured using a video tracking software (TopScan, CleverSys, Inc.). The object location preference (% of time with object) was calculated as the exploration time of the objects in the familiar or in the novel location/total exploration time.

Contextual fear conditioning test

This behavioral test was performed following a published protocol[53] with modifications. In this associative learning task, mice are presented with a neutral conditioned cue stimulus that is paired with an aversive unconditioned stimulus in a particular context. The mice learn that the chamber context and the cue stimulus predict the aversive stimulus and elicit a specific

behavioral response, namely freezing. Mice were brought into the testing room to acclimate for at least 30 minutes before testing. For the test, we used two Habitest® chambers (Coulbourn Instruments, Allentown, PA, USA) with stainless grid floors attached to a shock generator for foot shock delivery and dimly illuminated with a white fluorescent light bulb. The chambers were cleaned and made odor-free before starting the experiment and between each session (or each mouse). The fear conditioning test was conducted over 2 days. On day 1, mice were placed in the conditioning chamber and allowed to habituate for 3 minutes. Then, mice received three pairs of cue-aversive stimuli, consisting of tone (18 s, 5 kHz, 75 dB)-shock (2 s, 0.5 mA) pairings, separated by an interval of 40 s (total of 3 minutes). Mice were returned to their home cage 30 sec after the last shock presentation. On day 2, mice were tested and scored for conditioned fear to the training context for 3 minutes (context test), but with no presentation of the cue stimulus. Two hours later, mice were presented to a novel context, where the light intensity was slightly increased, the grid and walls of the chamber were covered by plastic inserts with different texture and colours and the inside of the chamber was scented with a paper towel dabbed with vanilla extract placed under the floor grid. In this last session, mice were placed in the conditioning chamber and allowed to habituate for 3 minutes, after which they received a continuous cue stimulus (tone) for an additional 3 minutes (cued test). Mice behaviour was recorded by a digital video camera mounted above the conditioning chamber and freezing was manually scored by a blinded experimenter using the Etholog V2.2 software. Parameters analysed included the percentage of time freezing during the 3 minutes of the context test and the last 3 minutes of the cued test.

MWM test

The Morris water maze test was performed as described before[53], but with modifications. Mice were transported to the behavior room to habituate at least 30 min before starting the test. The MWM test consisted of 4 days of acquisition, 1 day of probe trial and 2 days of reversal. In the acquisition, mice performed four trials per day, for 4 consecutive days, to find a hidden 10-cm diameter platform located 1 cm below the water surface in a pool 1 m in diameter. Tap water was made opaque with nontoxic tempera white paint and the water temperature was kept at 23 ± 1°C. A dim light source was placed within the testing room and only distal visual cues were available above each quadrant of the swimming pool to aid in the spatial navigation and location of the submerged platform. The latency to platform, i.e., the time required by the mouse to find and climb onto the platform, was recorded for up to 60 s. Each mouse was allowed to remain on the platform for 20 s and was then moved from the maze to its home cage. If the mouse did not find the platform within 60 s, it was manually placed on the platform and returned to its home cage after 20 s. The inter-trial interval for each mouse was of at least 5 min. On day 5, the platform was removed from the pool, and each mouse was tested in a probe trial for 60 s. On days 1 and 2 of the reversal, without changing the position of the visual cues, the platform was placed in the quadrant opposite to the original acquisition quadrant and the mouse was retrained for four trials per day. All MWM testing was performed between 1 p.m. and 6 p.m., during the lights-on phase, by a blinded experimenter. During the acquisition, probe and reversal, data were recorded using the EthoVision automated tracking system (Noldus Information Technology). The mean latency (in s) of the four trials was calculated for each day of test. The % of time

in the platform quadrant was calculated for the probe trial. Additionally, using a modified version of previous published methods[54,55], the full tracked path taken by each mouse in every trial of the acquisition and reversal days was used to classify the type of navigation strategy as either egocentric or allocentric by a blinded experimenter. The mean % of allocentric navigation of four trials was calculated for each day.

CSF and tissue collection and processing

Mice were given a lethal dose of anesthetics by intraperitoneal (i.p.) injection of Euthasol (10% v/v in saline). When needed, CSF was collected from the cisterna magna using a 0.5 mm diameter borosilicate glass pipette with internal filament and immediately stored at −80°C. Mice were then transcardially perfused with ice cold PBS with heparin (10 U/mL). Deep cervical lymph nodes were dissected and drop fixed in 4% paraformaldehyde (PFA) for 12 hours at 4°C. After stripping the skin and muscle from the bone the head was collected and drop fixed in 4% PFA. After removal of the mandibles and the skull rostral to maxillae, the top of the skull (skullcap) was removed with surgical curved scissors by cutting clockwise, beginning and ending inferior to the right post-tympanic hook and kept in PBS 0.02 % azide at 4°C until further use. The brains were kept in 4% PFA for additional 24 hours (48 hours in total). Fixed brain and dCLNs were then washed with PBS, cryoprotected with 30% sucrose and frozen in Tissue-Plus® O.C.T. compound (Thermo Fisher Scientific). Fixed and frozen brains were sliced (100 μm thick sections) with a cryostat (Leica) and kept in PBS 0.02 % azide at 4°C. Frozen lymph nodes were sliced (30 μm thick sections) in a cryostat, collected into gelatin-coated Superfrost™ Plus slides (Thermo Fisher Scientific) and stored at −20°C. Alternatively, after euthanizing and perfusing the mouse, the skullcap was removed from the mouse's head and drop fixed in 4% PFA for 12 hours, and the brains were immediately collected into O.C.T. compound, snap frozen in dry ice and stored at −80°C. Fresh frozen brains were then sliced (30 μm thick sections) in the cryostat and sections were directly collected into Superfrost™ Plus slides and kept at −20°C until further use. Fixed meninges (dura mater and arachnoid) were carefully dissected from the skullcaps with Dumont #5 forceps (Fine Science Tools) and kept in PBS 0.02 % azide at 4°C until further use.

Aβ measurement in CSF

To measure the concentration of $A\beta_{1\text{-}37/42}$ peptides in the CSF of J20 mice an in-house direct ELISA assay was used. Briefly, Nunc MaxiSorp® flat-bottom 96-well plates (ThermoFisher Scientific) were coated with 2 μL of CSF diluted in 98 μL of a KH_2PO_4/K_2HPO_4 buffer (pH 8.0) solution (1:50 dilution factor), for 2 h at 37°C. After washing with PBS 0.05% Tween® 20 (Sigma-Aldrich), a blocking step with PBS 1 % skim milk was performed for 1 h at room temperature (RT). Then, consecutive incubations for 1 h at RT were performed: first with rabbit anti-$A\beta_{1\text{-}37/42}$ (Cell Signaling, clone D54D2, 1:500), second with biotinylated goat anti-rabbit (Vector Laboratories, BA-1000, 1:500) and third with streptavidin-horseradish peroxidase (1:2500, Sigma-Aldrich). Each incubation step was separated by thorough washes with PBS 0.05% Tween® 20 and PBS. Finally, a citrate-phosphate buffer (pH 4.3) solution containing 0.1 % of 2,2′-azino-bis(3-ethylbenzothiazoline-6-sulfonic acid) diammonium salt (ABTS, Sigma-Aldrich) was added to each well and absorbance was read at 405 nm. The standard curve used to extrapolate the

concentration of $A\beta_{1\text{-}37/42}$ in the CSF was obtained using known concentrations of human $A\beta_{42}$ (AnaSpec, Inc.) that ranged from 0.1 to 100 ng/mL (considering the linearity of the assay). Data processing was done with Excel and statistical analysis performed using Prism 7.0a (GraphPad Software, Inc.).

Human samples

Autopsy specimens of human brain and dura from non-AD ($n = 8$) or AD ($n = 9$) patients were obtained from the Department of Pathology at the University of Virginia. All samples were from consenting patients that gave no restriction to the use of their body for research and teaching (through an UVA's Institutional Review Board for Health Sciences Research). Diagnosis criteria and pathological score were performed following the National Institute on Aging/Alzheimer's Association guidelines[56], based on the ABC (Amyloid, Braak, CERAD) score, for seven of the AD cases; old guidelines were used to diagnose and score two of the AD cases (Extended data Table 1). All obtained samples were fixed in a 20% formalin solution and kept in paraffin blocks until further sectioning. Prior to immunohistochemical staining, slides containing 10 μm thick sections were heated to 70°C for 30 min and de-paraffinized by washing sections with xylene, xylene 1:1 100% ethanol (v/v), and 100, 95, 70 and 50% ethanol in water. Finally tissue sections were rehydrated by rinsing with cold tap water.

Immunohistochemistry, imaging and quantifications

Mouse fresh frozen brain sections were fixed with 4% PFA for 30 min, rinsed in dH_2O and submitted to a heat-induced antigen retrieval step with 10 mM citrate buffer for 20 min. After de-paraffinization, sections of human brain or dura were submitted to the same antigen retrieval step for 20 min. The steps described next were generally applied for mouse fresh frozen or fixed free-floating brain sections, lymph node sections on slide, meningeal whole-mounts and human fixed tissue. For immunofluorescence staining, tissue was rinsed in PBS and washed with PBS 0.5% Triton-X-100 for 10 min, followed by incubation in PBS 0.5% Triton-X-100 containing 0.5% of normal serum (either goat or chicken) and 0.5% bovine serum albumin (BSA) for 1 hour at RT. This blocking step was followed by incubation with appropriate dilutions of primary antibodies: anti-LYVE-1 eFluor 660 or anti-LYVE-1 Alexa Fluor® 488 (eBioscience, clone ALY7, 1:200), anti-CD31 (Millipore Sigma, MAB1398Z, clone 2H8, 1:200), anti-IBA1 (Abcam, ab5076, 1:300), anti-GFAP (Millipore Sigma, ab5541, 1:300), anti-AQP4 (Millipore Sigma, A5971, 1:200), anti-Ki67 (Abcam, ab15580, 1:100), anti-$hA\beta_{1\text{-}16}$ (BioLegend, clone 6E10, 1:200), anti-$A\beta_{1\text{-}37/42}$ (Cell Signaling, clone D54D2, 1:300) and anti-GFP (Abcam, ab6556, 1:300) in PBS 0.5% Triton-X-100 containing 0.5% of normal serum and 0.5% BSA overnight at 4°C. Meningeal whole-mounts or tissue sections were then washed 3 times for 5 min at RT in PBS 0.5% Triton-X-100 followed by incubation with the appropriate chicken, goat or donkey Alexa Fluor® 488, 546, 594, or 647 anti-rat, -goat, -rabbit, -mouse or -Armenian hamster IgG antibodies (Thermo Fisher Scientific, 1:500) for 1 or 2 hours at RT in PBS 0.5% Triton-X-100. After an incubation for 10 min with 1:2000 DAPI in PBS, the tissue was washed 3 times for 5 min with PBS at RT and mounted with Aqua-Mount (Lerner) and glass coverslips. Preparations were stored at 4°C for no more than 1 week until images were acquired either using a widefield microscope (Leica) or a confocal microscope (FV1200 Laser Scanning Confocal Microscope, Olympus).

Quantitative analysis using the acquired images was performed on FIJI software. For the assessment of brain fluorescent tracer influx or efflux or AQP4 coverage, 10 representative brain sections were imaged using the widefield microscope and the mean area fraction was calculated using Microsoft Excel. For lymph nodes, the area fraction of drained fluorescent tracer or lymphatic vessels was assessed in alternate sections (representing a total of 10–15 sections per sample) using the confocal microscope and the mean was calculated for each sample. Area of coverage by $CD31^+$ blood vessels and $AQP4^+$ astrocyte endfeet in the brain cortex was achieved by calculating the mean value of 10 representative fields (5 images in each cerebral hemisphere) per sample acquired using the confocal microscope. For lymphatic vessel diameter, images of the same region of the superior sagittal sinus or of the transverse sinus were acquired in the confocal microscope and the mean of 100 individual lymphatic vessel diameter measurements (50 measurements in each lymphatic vessel lining the sinus using FIJI) was calculated for each sample by a blinded experimenter (due to different criteria used by distinct experimenters, this quantification method is often associated with a variability of ± 15% in absolute diameter values). For assessment of meningeal lymphatic vessel coverage and complexity, images of meningeal whole-mounts were acquired in the confocal microscope and FIJI was used for quantifications. When applicable, the same images were used to assess the % of field coverage by $LYVE\text{-}1^-CD31^+$ vessels. To quantify the number of proliferating $Ki67^+$ cells in the hippocampal dentate gyrus, images of the entire dentate gyrus of 3 representative brain sections per sample were obtained using the confocal microscope. Fiji was used to assess the number of $Ki67^+$ per mm^2 of DAPI cells that composed the granular zone, which were then used to calculate the average density of cells per sample. For assessment of amyloid burden in the dorsal hippocampus, tile scans of the entire dorsal hippocampus from 10 coronal brain sections (~180 μm apart from each other) were obtained using the confocal microscope. FIJI was used to quantify amyloid plaque size, number and total coverage.

Flow Cytometry

Mice were injected i.p. with Euthasol solution and were then transcardially perfused with ice cold PBS with heparin. Individual meninges were immediately dissected from the mouse's skull cap and digested 15 min at 37°C with 1.4 U/ml of Collagenase VIII (Sigma Aldrich) and 35 U/ml of DNAse I (Sigma Aldrich) in complete media consisting of DMEM (Gibco) with 2% FBS (Atlas Biologicals), 1% L-Glutamine (Gibco), 1% penicillin/streptomycin (Gibco), 1% Sodium pyruvate (Gibco), 1% non-essential amino-acid (Gibco) and 1.5% Hepes (Gibco). The cell pellets were washed, resuspended in ice-cold fluorescence-activated cell sorting (FACS) buffer (pH 7.4; 0.1 M PBS; 1 mM EDTA and 1% BSA) and stained for extracellular markers with the following antibodies: rat anti-CD90.2 FITC (553013; BD Bioscience), rat anti-CD11b FITC (557396; BD Bioscience), rat monoclonal anti-CD19 PE (12-0193-82; eBioscience), rat anti-CD45 PerCP-Cy5.5 (550994; BD Bioscience), rat anti-Ly6C PerCP-Cy5.5 (560525; BD Bioscience), mouse anti-NK1.1 PE-Cy7 (552878; BD Bioscience), rat anti-Ly6G PE-Cy7 (560601; BD Bioscience), rat anti-CD4 APC (553051; BD Bioscience), rat anti-CD45 AF700 (560510; BD Bioscience), hamster anti-TCRb BV711 (563135; BD Bioscience), rat anti-CD8 Pacific blue (558106; BD Bioscience) and rat anti-Siglec-F BV421 (562681; BD Bioscience). Cell viability was determined by using the Zombie Aqua™ Fixable Viability Kit following the manufacturer's instructions

(BioLegend). After an incubation period of 30 min at 4°C, cells were washed and fixed in 1% PFA in PBS. Fluorescence data was collected with a Gallios™ Flow Cytometer (Beckman Coulter, Inc.) then analyzed using FlowJo software (Tree Star, Inc.). Briefly, singlets were gated using the height, area and the pulse width of the forward and side scatter and then viable cells were selected as $AQUA^-$. Cells were then gated for the appropriate cell type markers. An aliquot of unstained cells of each sample was counted using Cellometer Auto2000 (Nexcelor) to provide accurate counts for each population. Data processing was done with Excel and statistical analysis performed using Prism 7.0a (GraphPad Software, Inc.).

Sorting of meningeal LECs

To obtain a suspension of meningeal lymphatic endothelial cells (LECs) from the meninges of young-adult (2–3 months) and old (20–24 months) mice by FACS, mice were euthanized by i.p. injection of Euthasol and transcardially perfused with ice cold PBS with heparin. Skullcaps were quickly collected and meninges (dura mater and arachnoid) were dissected using Dumont #5 forceps in complete media composed of DMEM (Gibco) with 2% FBS (Atlas Biologicals), 1% L-glutamine (Gibco), 1% penicillin/streptomycin (Gibco), 1% sodium pyruvate (Gibco), 1% non-essential amino-acids (Gibco) and 1.5% Hepes buffer (Gibco). Individual meninges were then incubated with 1 mL of complete media with 1.4 U/mL of Collagenase VIII (Sigma-Aldrich) and 35 U/mL of DNAse I (Sigma-Aldrich) for 15 min at 37°C. Individual samples consisted of cell suspensions pooled from 10 meninges that were obtained after filtration through a 70 μm nylon mesh cell strainer. Cell suspensions were then pelleted, resuspended in ice-cold FACS buffer containing DAPI (1:1000, Thermo Fisher Scientific), anti-CD45-BB515 (1:200, clone 30-F11, BD Biosciences), anti-CD31-Alexa Fluor® 647 (1:200, clone 390, BD Biosciences) and anti-Podoplanin-PE (1:200, clone 8.1.1, eBioscience) and incubated for 15 min at 4°C. Cells were then washed and resuspended in ice-cold FACS buffer. Briefly, singlets were gated using the pulse width of the side scatter and forward scatter. Cells negative for DAPI were selected for being viable cells. The LECs were then gated as $CD45^-CD31^+Podoplanin^+$ (see Extended data Fig. 6 for representative dot plots) and sorted into a 96-well plate containing 100 μL of lysis buffer (Arcturus PicoPure RNA Isolation Kit, Thermo Fisher Scientific) using the Influx™ Cell Sorter (BD Biosciences) that is available at the University of Virginia Flow Cytometry Core Facility.

RNA extraction and sequencing

For total RNA extraction from whole hippocampus, the tissue was macrodissected from the brain in ice-cold PBS, immersed in the appropriate volume of extraction buffer from the RNA isolation kit, immediately snap frozen in dry ice and stored at −80°C until further use. After defrosting in ice, samples were mechanically dissociated in extraction buffer and RNA was isolated using the kit components according to the manufacturer's instructions (RNeasy mini kit, cat. no. 74106, Qiagen). The Illumina TruSeq Stranded Total RNA Library Prep Kit was used for cDNA library preparation from total RNA samples. Sample quality control was performed on an Agilent 4200 TapeStation Instrument, using the Agilent D1000 kit, and on the Qubit Fluorometer (Thermo Fisher Scientific). For RNA sequencing (RNA-seq),

libraries were loaded on to a NextSeq 500 (Illumina) using an Illumina NextSeq High Output (150 cycle) cartridge (#FC-404-2002).

Total RNA was extracted from LECs (previously sorted by FACS) using the Arcturus PicoPure RNA Isolation Kit (Thermo Fisher Scientific), following the manufacturer's instructions. All RNA sample processing (including linear RNA amplification and cDNA library generation) and RNA-seq was performed by HudsonAlpha Genomic Services Laboratory (Huntsville, AL).

The raw sequencing reads (FASTQ files) were first chastity filtered, which removes any clusters that have a higher than expected intensity of the called base compared to other bases. The quality of the reads was then evaluated using FastQC[57], and after passing quality control (QC), the expression of the transcripts was quantified against the UCSC mm10 genome[58] using Salmon[59]. These transcript abundances were then imported into R and summarized with tximport[60], and then DESeq2[61] was used to normalize the raw counts, perform exploratory analysis (e.g., principal component analysis), and to perform differential expression (DE) analysis. Before DE analysis of the meningeal LECs from adult vs old mice dataset, surrogate variable analysis[62] (SVA) was used to identify and adjust for latent sources of unwanted variation as implemented in the SVA package[63]. The *P*-values from the DE analysis were corrected for multiple hypothesis testing with the Benjamini–Hochberg false discovery rate procedure (adj. *P*-value). Functional enrichment of DE genes, using gene sets from Gene Ontology (GO) and Kyoto Encyclopedia of Genes and Genomes (KEGG), was determined with Fisher's exact test as implemented in the clusterProfiler[64] Bioconductor package. Heatmaps of the DE genes and enriched gene sets were generated with the R package pheatmap[65]. Normalized counts of selected transcripts were used to calculate the fold change relative to respective controls.

Statistical analysis and reproducibility

Sample sizes were chosen on the basis of standard power calculations (with $\alpha = 0.05$ and power of 0.8) performed for similar experiments that were previously published. In general, statistical methods were not used to re-calculate or predetermine sample sizes. The Kolmogorov-Smirnov test was used to assess normal distribution of the data. Variance was similar within comparable experimental groups. Animals from different cages, but within the same experimental group, were selected to assure randomization. Experimenters were blinded to the identity of experimental groups from the time of euthanasia until the end of data collection and analysis for at least one of the independent experiments. Statistical tests for each figure were justified to be appropriate. One-way ANOVA, with Bonferroni's post-hoc test or Holm-Sidak's post-hoc test, was used to compare 3 independent groups. Two-group comparisons were made using two-tailed unpaired Mann-Whitney test. For comparisons of multiple factors (for example, age *vs* treatment), two-way ANOVA with Bonferroni's post-hoc test was used. Repeated measures two-way ANOVA with Bonferroni's post-hoc test was used for day *vs* treatment comparisons with repeated observations. Statistical analysis (data was always presented as mean ± s.e.m.) was performed using Prism 7.0a (GraphPad Software, Inc.).

Reporting summary

Further information on experimental design is available in the Nature Research Reporting Summary linked to this paper.

Code and data availability

Source data for quantifications mentioned either in the text or shown in graphs plotted in Figs. 1–3 and Extended data Figs. 1–9 are available in the online version of this paper at www.nature.com/nature. RNA-seq data sets have been deposited online in the Gene Expression Omnibus (GEO database) under the accession numbers GSE104181, GSE104182 and GSE113351. Lymph4D software code is available online under GNU General Public license v3.0 at https://github.com/avaccari/Lymph4D. Custom code used and datasets generated and/or analyzed during the current study are also available from the corresponding authors upon reasonable request.

Extended Data

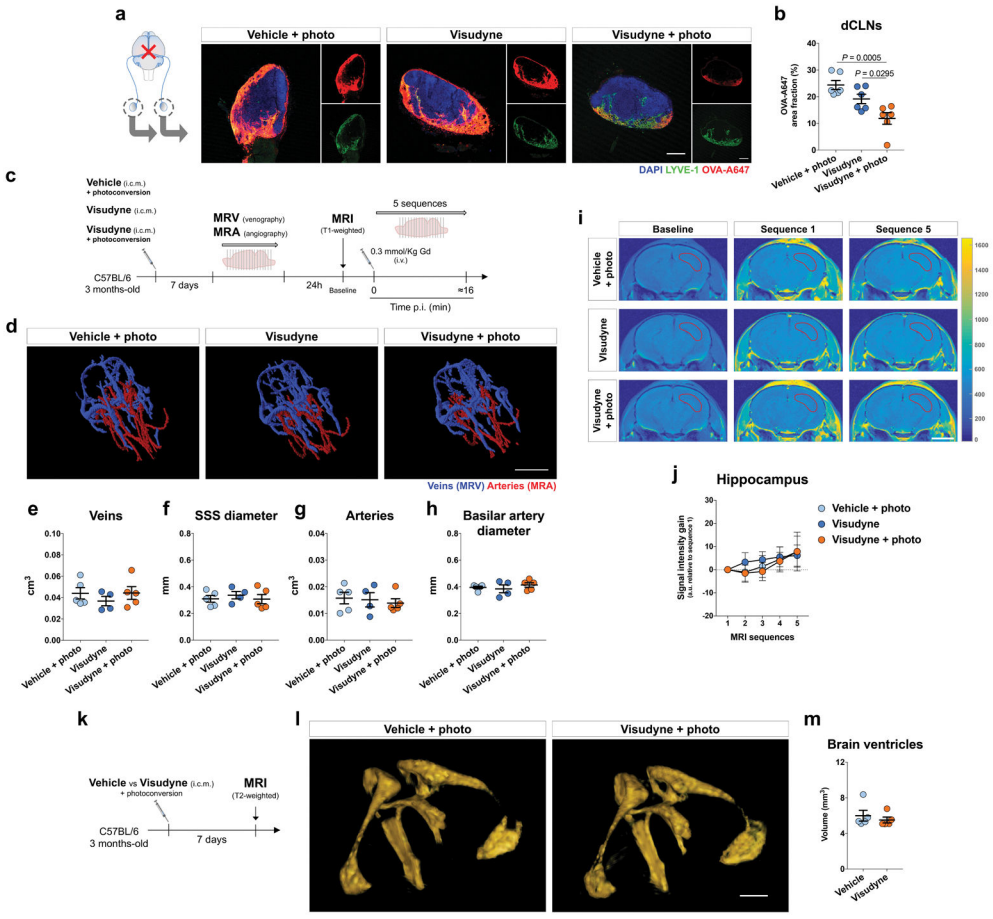

Extended Data Figure 1. Ablation of meningeal lymphatics leads to decreased CSF macromolecule drainage without affecting meningeal/brain blood vasculature or brain ventricular volume

a, Seven days after meningeal lymphatic ablation, a volume of 5 μL of fluorescent ovalbumin-Alexa647 (OVA-A647) was injected intra-cisterna magna (i.c.m.), into the CSF, and drainage of tracer into the deep cervical lymph nodes (dCLNs) was assessed 2 h later. Representative images of OVA-A647 (red) drained into the dCLNs stained for LYVE-1 (green) and with DAPI (blue; scale bar, 200 μm). **b,** Quantification of OVA-A647 area fraction (%) in the dCLNs showed significantly less amount of tracer in the Visudyne/photoconversion group than in control groups (mean ± s.e.m., $n = 6$ per group; one-way ANOVA with Bonferroni's post-hoc test; **a** and **b** is representative of 2 independent experiments; significant differences between vehicle/photoconversion and Visudyne/photoconversion groups were observed in a total of 5 independent experiments). **c,** Seven days after meningeal lymphatic ablation, mice from the 3 groups were submitted to magnetic resonance venography (MRV) or angiography (MRA) and 24 h later to T2-weighted MRI to assess blood-brain barrier integrity after i.v. injection of the contrast agent gadolinium (Gd) at a dose of 0.3 mmol/Kg. **d,** Representative 3D reconstructions of intracranial veins and arteries of mice from each group (scale bar, 5 mm). **e–h,** No significant changes between groups were observed for (**e**) venous vessel volume, (**f**) superior sagittal sinus (SSS) diameter, (**g**) arterial vessel volume and (**h**) basilar artery diameter (mean ± s.e.m., $n = 5$ in vehicle/photoconversion and in Visudyne/photoconversion, $n = 4$ in Visudyne; one-way ANOVA with Bonferroni's post-hoc test). **i,** Using the Lymph4D software, it was possible to measure changes in signal intensity gain in MRI sequences 1–5 (relative to baseline) in the hippocampus of mice from each group (scale bar, 3 mm). **j,** Quantification of the signal intensity gain (relative to baseline) in the hippocampus over 5 MRI acquisition sequences showed no differences between groups (mean ± s.e.m., $n = 5$ in vehicle/photoconversion and in Visudyne/photoconversion, $n = 4$ in Visudyne; repeated measures two-way ANOVA with Bonferroni's post-hoc test). **k,** Mice were subjected to T2-weighted MRI to assess volume changes in brain ventricles 7 days after injection of vehicle or Visudyne and photoconversion. **l,** Representative images of 3D reconstruction of brain ventricles of mice from the two groups (scale bar, 1 mm). **m,** No differences were detected in the volume of the brain ventricles after meningeal lymphatic ablation (mean ± s.e.m., $n = 5$ per group; two-tailed Mann-Whitney test).

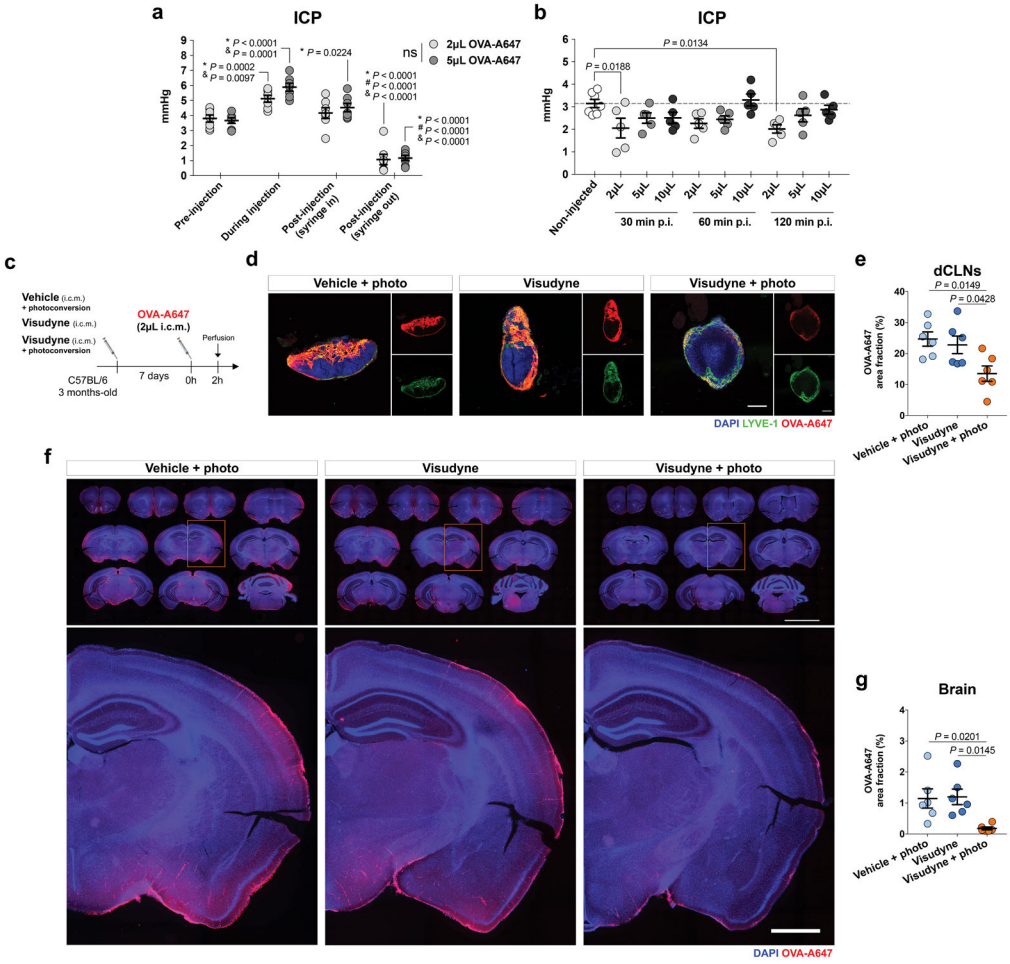

Extended Data Figure 2. Intracranial pressure measurements and assessment of CSF drainage and brain influx

a, Intracranial pressure (ICP) was measured in four different steps of intra-cisterna magna (i.c.m.) injection of 2 µL or 5 µL of tracer solution: pre-injection, during injection, post-injection (with syringe inside the cisterna magna) and post-injection (with syringe out of the cisterna magna). A significant increase in ICP for each volume was observed during injection when compared to pre-injection and post-injection (syringe in). Significantly higher ICP values post-injection (syringe in) were observed when compared to ICP values pre-injection. A significant decrease in ICP for each volume was observed post-injection (syringe out) when compared to all other steps of i.c.m. injection. No significant differences in ICP values were observed between groups injected with 2 µL or 5 µL of tracer for any of the analyzed steps of the i.c.m. injection method (mean ± s.e.m., $n = 7$ per group; repeated measures two-way ANOVA with Bonferroni's post-hoc test; *vs pre-injection; $^{\#}$vs during injection; $^{\&}$vs post-injection (syringe in); data was pooled from 2 independent experiments). **b,** ICP was measured 30, 60 and 120 min post injection (p.i.) of 2, 5 or 10 µL of tracer solution into the CSF and compared to ICP values in non-injected mice. Significant differences were observed between ICP values of non-injected mice and mice injected with 2 µL of tracer at 30 min and 120 min post-injection (mean ± s.e.m., $n = 5$ per group; one-way ANOVA with Bonferroni's post-hoc test). **c,** Seven days after meningeal lymphatic

ablation, a volume of 2 μL of fluorescent OVA-A647 was injected into the CSF and drainage of tracer into the dCLNs was assessed 2 h later. **d,** Representative images of OVA-A647 (red) drained into the dCLNs, stained for LYVE-1 (green) and with DAPI (blue; scale bar, 200 μm). **e,** Quantification of OVA-A647 area fraction (%) in the dCLNs showed significantly less amount of tracer in the Visudyne/photoconversion group than in control groups. **f,** Representative brain sections stained with DAPI (blue) showing OVA-A647 (red) influx into the brain parenchyma of mice from Visudyne/photoconversion and control groups (scale bar, 5 mm; inset scale bar, 1 mm). **g,** Quantification of OVA-A647 area fraction (%) in brain sections showing a significant decrease in the Visudyne/photoconversion group when compared to control groups. Data in **e** and **g** is presented as mean ± s.e.m., $n = 6$ per group; one-way ANOVA with Bonferroni's post-hoc test was used in **e** and **g; c**–**g** is representative of 2 independent experiments.

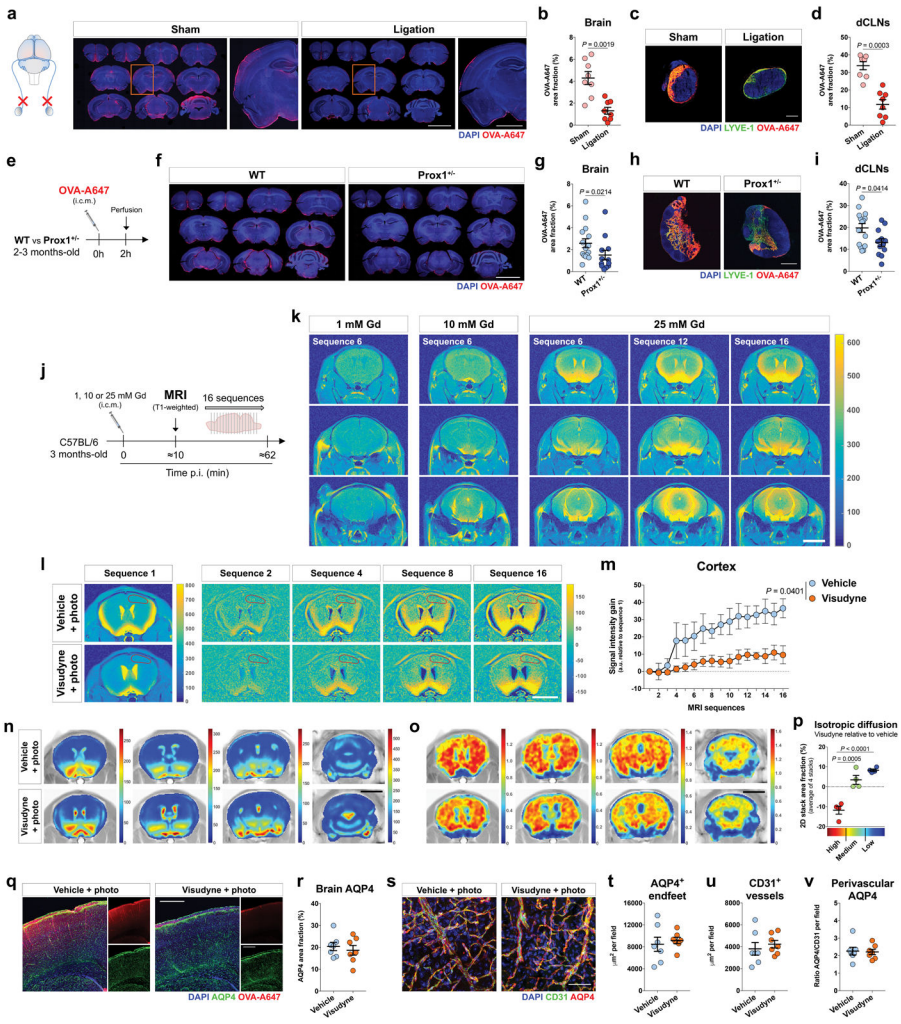

Extended Data Figure 3. Impaired brain perfusion by CSF macromolecules is observed in lymphatic ligated and in Prox1$^{+/-}$ mice and does not correlate with AQP4 levels

a, Adult mice were submitted to surgical ligation of the lymphatic vessels afferent to the dCLNs. One week after the procedure, 5 μL of OVA-A647 was injected into the CSF (i.c.m.)

and mice were transcardially perfused 2 h later. Representative brain sections stained with DAPI (blue) showing OVA-A647 (red) influx into the brain parenchyma of ligated and sham-operated mice (scale bar, 5 mm; inset scale bar, 2 mm). **b,** Quantification of OVA-A647 area fraction (%) in brain sections showed a significant decrease in the ligation group. **c,** Representative sections of dCLNs stained with DAPI (blue) and for LYVE-1 (green), showing OVA-A647 (red) coverage in the ligation and sham-operated groups (scale bar, 200 μm). **d**, Quantification of OVA-A647 area fraction (%) in the dCLNs showed a significant decrease in the ligation group. Data in **b** and **d** is presented as mean ± s.e.m., $n = 8$ per group; two-tailed Mann-Whitney test was used in **b** and **d**; data in **a**–**d** was pooled from 2 independent experiments and is representative of 3 independent experiments. **e**, Wild-type (WT) and Prox1$^{+/-}$ mice (2–3 months-old) were injected with 5 μL of OVA-A647 into the CSF (i.c.m.) and transcardially perfused 2 h later. **f,** Representative brain sections stained with DAPI (blue) showing OVA-A647 (red) influx into the brain parenchyma of Prox1$^{+/-}$ and WT mice (scale bar, 5 mm). **g,** Quantification of OVA-A647 area fraction (%) in brain sections showed a significant decrease in Prox1$^{+/-}$ mice. **h,** Representative sections of dCLNs stained with DAPI (blue) and for LYVE-1 (green), showing OVA-A647 (red) coverage in the dCLNs of Prox1$^{+/-}$ and WT mice (scale bar, 500 μm). **i,** Quantification of OVA-A647 area fraction (%) in the dCLNs showed a significant decrease in Prox1$^{+/-}$ mice. Data in **g** and **i** is presented as mean ± s.e.m., $n = 15$ in WT, $n = 12$ in Prox1$^{+/-}$; two-tailed Mann-Whitney test was used in **g** and **i;** data in **e**–**i** was pooled from 2 independent experiments. **j,** Rate of brain paravascular influx of the contrast agent gadolinium (Gd), injected i.c.m. at 1, 10 or 25 mM (in saline), was assessed in adult mice (3 months-old) by T1-weighted magnetic resonance imaging (MRI). **k,** Representative MRI images obtained using Lymph4D software showing brain signal intensity for different concentrations of injected Gd (scale bar, 3 mm). Experiment in **j** and **k** was performed once. **l,** Adult mice were subjected to meningeal lymphatic ablation by Visudyne photoconversion. One week later, T1-weighted MRI acquisition was performed after i.c.m. injection of 5 μL of Gd (25 mM in saline). Using the Lymph4D software, it was possible to measure the rate of contrast agent influx into the delineated brain cortical region of mice from both groups (scale bar, 3 mm). Images in sequence 2 and subsequent were obtained by subtraction of sequence 1. **m,** Quantification of the signal intensity gain (relative to sequence 1) in the brain cortex revealed a significant decrease in the Visudyne/photoconversion group, when compared to vehicle/photoconversion. **n, o,** Coronal sections of the brain of vehicle- or Visudyne-treated mice ($n = 4$ per group) were aligned and stacked into 2D colormaps (concatenated from 16 MRI sequences) showing (**n**) contrast of Gd signal intensity and (**o**) isotropic diffusion coefficient (scale bars, 3 mm). **p,** Area fraction quantification of high, medium and low values of isotropic diffusion coefficient in the four 2D stacks, in Visudyne relative to vehicle. Data in **m** and **p** is presented as mean ± s.e.m., $n = 4$ per group; repeated measures two-way ANOVA with Bonferroni's post-hoc test was used in **m** and one-way ANOVA with Bonferroni's post-hoc test was used in **p; l**–**p** is representative of 2 independent experiments. **q,** Representative confocal images of DAPI (blue) and aquaporin 4 (AQP4, green) staining and OVA-A647 (red) levels in brain sections from vehicle- and Visudyne-treated mice (scale bar, 500 μm). **r,** Quantification of area fraction (%) of AQP4 in the brains of mice treated with vehicle or Visudyne showing no differences between groups. **s,** Images showing representative staining for AQP4^{+} astrocytic endfeet (red) and CD31^{+} blood vessels (green)

in the brain cortex of mice from vehicle and Visudyne groups (scale bar, 50 μm). **t–v,** No changes were observed in the area of (**t**) AQP4$^+$ astrocytic endfeet and of (**u**) CD31$^+$ blood vessels or in (**v**) the ratio between area of AQP4$^+$ and of CD31$^+$. Data in **r** and **t–v** is presented as mean ± s.e.m., $n = 7$ per group; two-tailed Mann-Whitney test was used in **r** and **t–v**; data in **q–v** was pooled from 2 independent experiments and is representative of 3 independent experiments.

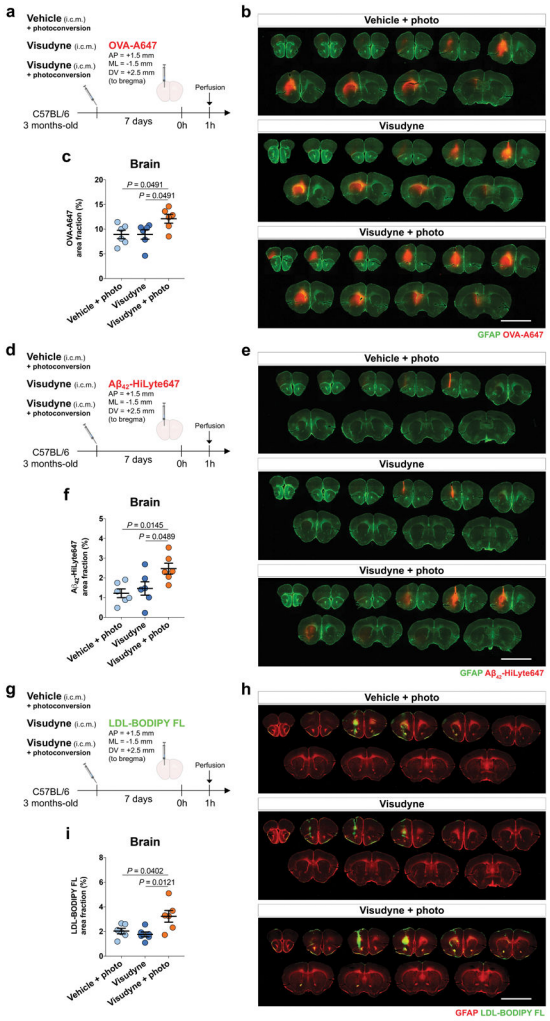

Extended Data Figure 4. Ablation of meningeal lymphatic vessels impairs efflux of macromolecules from the brain

a, Seven days after meningeal lymphatic ablation, 1 μL of fluorescent OVA-A647 (0.5 mg/mL in artificial CSF) was stereotaxically injected (coordinates from bregma, AP = +1.5 mm, ML = −1.5 mm, DV = +2.5 mm) into the brain parenchyma. **b,** Representative brain sections rostral and caudal to the injection site, stained for glial fibrillary acidic protein (GFAP, in green), demonstrating OVA-A647 (red) coverage of the brain parenchyma in the Visudyne/photoconversion group and the control groups (scale bar, 5 mm). **c,** Quantification of OVA-A647 area fraction (%) in the injected brain hemisphere showing a significantly higher level in the Visudyne/photoconversion group, when compared to both control groups

(mean ± s.e.m., n = 6 per group; one-way ANOVA with Bonferroni's post-hoc test). **d,** Seven days after meningeal lymphatic ablation, 1 μL of fluorescent $A\beta_{42}$-HiLyte647 (0.05 μg/mL in artificial CSF) was stereotaxically injected (coordinates from bregma, AP = +1.5 mm, ML = −1.5 mm, DV = +2.5 mm) into the brain parenchyma. **e,** Representative brain sections rostral and caudal to the injection site, stained for GFAP (green), demonstrating $A\beta_{42}$-HiLyte647 (red) coverage of the brain parenchyma in the Visudyne/photoconversion group and the control groups (scale bar, 5 mm). **f,** Quantification of $A\beta_{42}$-HiLyte647 area fraction (%) in the injected brain hemisphere showing a significantly higher level in the Visudyne/photoconversion group, when compared to both control groups (mean ± s.e.m., n = 6 per group; one-way ANOVA with Bonferroni's post-hoc test). **g,** Seven days after meningeal lymphatic ablation, 1 μL of fluorescent low density lipoprotein (LDL)-BODIPY FL (0.1 mg/mL in artificial CSF) was stereotaxically injected (coordinates from bregma, AP = +1.5 mm, ML = −1.5 mm, DV = +2.5 mm) into the brain parenchyma. **h,** Representative brain sections rostral and caudal to the injection site, stained for GFAP (red), demonstrating LDL-BODIPY FL (green) coverage of the brain parenchyma in the Visudyne/photoconversion group and the control groups (scale bar, 5 mm). **i,** Quantification of LDL-BODIPY FL area fraction (%) in the injected brain hemisphere showing a significantly higher level in the Visudyne/photoconversion group, when compared to both control groups (mean ± s.e.m., n = 6 per group; one-way ANOVA with Bonferroni's post-hoc test).

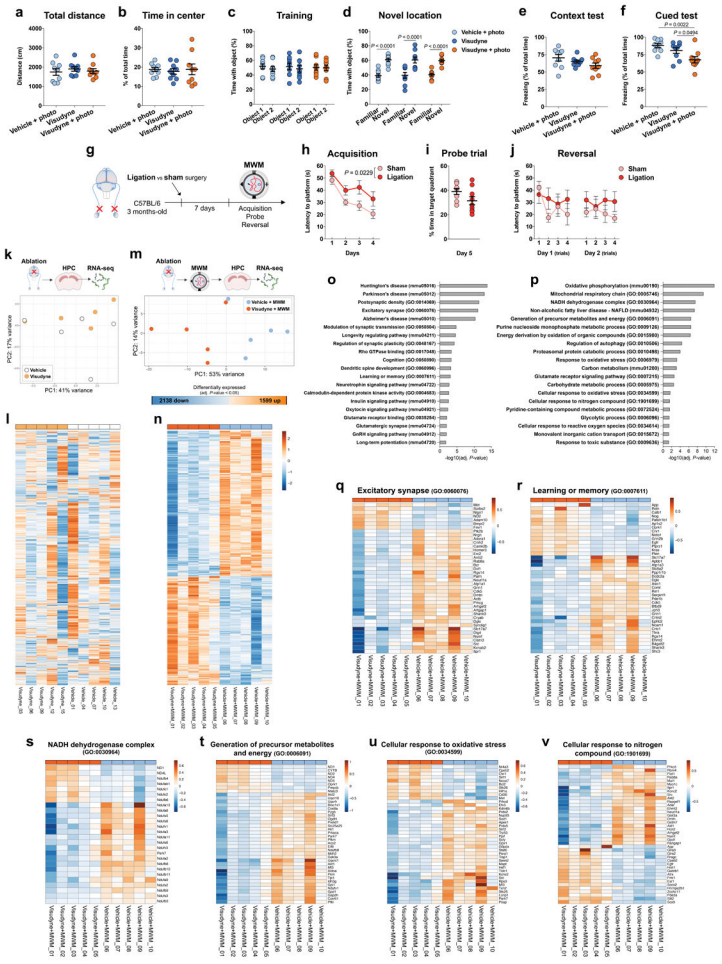

Extended Data Figure 5. Behavioral assessment and hippocampal RNA-seq analysis after impairing meningeal lymphatic function

a, b, No differences in (**a**) total distance and in (**b**) time in center of the open field arena were observed between vehicle/photoconversion, Visudyne and Visudyne/photoconversion groups (mean ± s.e.m., $n = 9$ per group; one-way ANOVA with Bonferroni's post-hoc test). **c, d,** Performance of mice from the 3 groups was also identical both in the (**c**) training and in the (**d**) novel location task of the novel location recognition paradigm (mean ± s.e.m., $n = 9$ per group; two-way ANOVA with Bonferroni's post-hoc test). **e, f,** Mice performance in the contextual fear conditioning paradigm showed no differences between groups in the (**e**) context test, but a statistically significant difference in the (**f**) cued test (mean ± s.e.m., $n = 9$ per group; one-way ANOVA with Bonferroni's post-hoc test). **g,** The cognitive performance of adult mice was assessed in the Morris water maze (MWM) test, one week after sham surgery or surgical ligation of the lymphatics afferent to the dCLNs. **h–j**, Ligated mice presented a significant increase in the (**h**) latency to platform during acquisition, when compared to sham-operated mice. No significant differences between groups were observed in the (**i**) % of time spent in the target quadrant in the probe trial or in the (**j**) reversal (mean ± s.e.m., $n = 8$ in sham, $n = 9$ in ligation; repeated measures two-way ANOVA with Bonferroni's post-hoc test was used in **h** and **j**; two-tailed Mann-Whitney test was used in **i**).

k, Vehicle or Visudyne injection with photoconversion were performed twice within two weeks interval. Total RNA was extracted from the hippocampus of mice from both groups and sequenced (RNA-seq). RNA-seq principal component (PC) analysis did not show a differential clustering of samples from vehicle and Visudyne groups. **l,** Heatmap showing relative expression levels of genes in vehicle/photoconversion and in Visudyne/photoconversion samples. **m,** After meningeal lymphatic ablation (twice within two weeks interval) and MWM performance, total RNA was extracted from the hippocampus of mice from vehicle/photoconversion or Visudyne/photoconversion groups and sequenced. RNA-seq principal component (PC) analysis demonstrating a differential clustering of samples from vehicle and Visudyne groups. A total of 2138 genes were down-regulated and 1599 genes were up-regulated in the hippocampus after meningeal lymphatic ablation and MWM performance. **n,** Heatmap showing relative expression levels of genes in vehicle/photoconversion and in Visudyne/photoconversion samples (color scale bar values represent standardized rlog-transformed values across samples for **l** and **n**). **o,** Neurological disease, neuronal activity and synaptic plasticity related GO and KEGG terms enriched upon Visudyne treatment, as measured by the –log10(adj. *P*-value). **p,** GO and KEGG terms related with metabolite generation and processing, glycolysis and mitochondrial respiration and oxidative stress that were enriched, as measured by the –log10(adj. *P*-value), upon Visudyne treatment and MWM performance. **q, r,** Heatmap showing relative expression levels of genes involved in two of the significantly altered GO terms related to (**q**) Excitatory synapse and (**r**) Learning or memory. **s–v,** Heatmaps showing relative expression levels of genes involved in four of the significantly altered GO terms related to (**s**) NADH dehydrogenase complex, (**t**) Generation of precursor metabolites and energy, (**u**) Cellular response to oxidative stress and (**v**) Cellular response to nitrogen compound. Datasets in **k–v** all consist of $n = 5$ per group; in **k** and **m** *P*-values were corrected for multiple hypothesis testing with the Benjamini–Hochberg false discovery rate procedure; in **l** and **n–v** functional enrichment of differential expressed genes was performed using gene sets from GO and KEGG and determined with Fisher's exact test; color scale bar values in **n** and **q–v** represent standardized rlog-transformed values across samples.

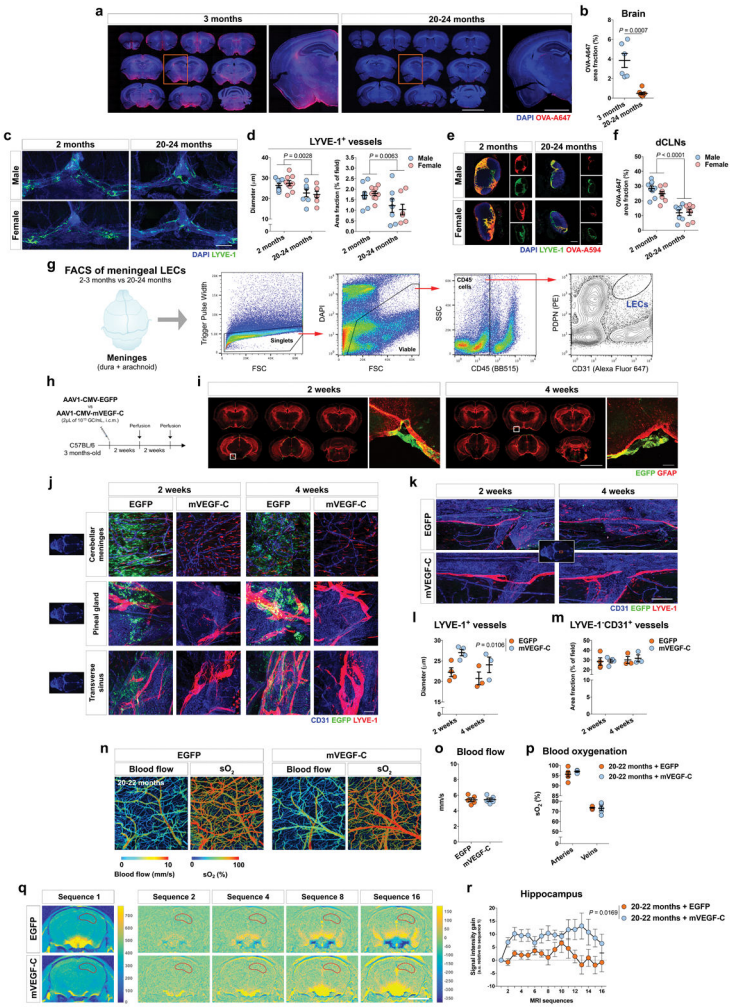

Extended Data Figure 6. Characterization of meningeal lymphatics in young and old mice and improvement of lymphatic function by viral-mediated expression of mVEGF-C

a, OVA-A647 was injected into the CSF (i.c.m.) of young-adult (3 months of age) and old (20–24 months of age) mice. Representative brain sections stained with DAPI (blue) showing degree of OVA-A647 (red) influx into the parenchyma (scale bar, 5 mm; inset scale bar, 2 mm). **b,** Quantification of OVA-A647 area fraction (%) in brain sections (mean ± s.e.m., $n = 6$ in 3 months, $n = 8$ in 20–24 months; two-tailed Mann-Whitney test; representative of 2 independent experiments). **c,** Representative images of DAPI (blue) and LYVE-1 (green) staining in meningeal whole-mounts of young-adult (2 months-old) and old (20–24 months-old) male and female mice (scale bar, 1 mm). **d,** Measurement of LYVE-1$^+$ vessel diameter and area fraction showed a significant decrease in both parameters in old mice, when compared to young-adults, in both females and males. **e,** Representative images of DAPI (blue) and LYVE-1 (green) staining in dCLNs 2 h after injection of OVA-A594 (red) into the CSF of young-adult and old mice from both genders (scale bar, 200 μm). **f,** Quantification of OVA-A594 area fraction (%) in the dCLNs of mice from different ages and genders showed a significant decrease in 20–24 months-old female and male mice. Data in **d** and **f** is presented as mean ± s.e.m., $n = 9$ per group at 2 months, $n = 7$ per group at 20–24

months for male and female; two-way ANOVA with Bonferroni's post-hoc test was used in **d** and **f**; data was pooled from 2 independent experiments. **g,** Representative dot and contour plots showing the gating strategy used to isolate meningeal lymphatic endothelial cells (LECs) by fluorescence-activated cell sorting (FACS) from the meninges of young-adult and old mice ($n = 3$ per group, pooled from 2 independent experiments). **h,** Adult mice were injected i.c.m. with 2 μL of AAV1-CMV-EGFP (EGFP) or AAV1-CMV-mVEGF-C (mVEGF-C), both at 10^{13} genome copies (GC)/mL, and transcardially perfused with saline 2 or 4 weeks later. **i,** Representative brain coronal sections of mice showing $EGFP^+$ infected cells (green) in the pia mater, surrounding the $GFAP^+$ glia limitans (red) of the brain parenchyma, at 2 and 4 weeks post injection (scale bar, 5 mm; inset scale bar, 200 μm). **j,** Representative insets from meningeal whole-mounts stained for CD31 (blue), EGFP (green) and LYVE-1 (red; scale bar, 200 μm). Green cells are observed in the cerebellar meninges, pineal gland and transverse sinus in the EGFP group at 2 and 4 weeks, but not in the same regions of the meninges in the mVEGF-C group. **k,** Representative images of $LYVE\text{-}1^+$ lymphatic vessels (red) and $LYVE\text{-}1^-CD31^+$ blood vessels (blue) in the superior sagittal sinus of mice treated with either EGFP or mVEGF-C, for 2 or 4 weeks (scale bar, 200 μm). **l, m,** Mice treated with AAV1 expressing mVEGF-C presented a significant increase in (**l**) lymphatic vessel diameter, but not in (**m**) coverage by blood vessels. Data in **l** and **m** is presented as mean ± s.e.m., $n = 4$ per group at 2 weeks, $n = 3$ per group at 4 weeks; two-way ANOVA with Bonferroni's post-hoc test was used in **l** and **m**; data in **h**–**m** is representative of 2 independent experiments. **n,** Representative images of blood flow (mm/s) and arterial and venous blood oxygenation (% of sO_2) readings obtained by Photoacoustic imaging of brain/meningeal vasculature of old mice (20–22 months-old) treated for 1 month with EGFP or mVEGF-C virus (both at 10^{13} GC/mL). **o, p,** The different treatments did not affect (**n**) blood flow or (**p**) blood oxygenation in the brain/meninges of old mice (mean ± s.e.m., $n = 5$ per group; two-tailed Mann-Whitney test was used in **n** and two-way ANOVA with Bonferroni's post-hoc test was used in **p**; data results from a single experiment). **q,** Old mice (20–22 months-old) were injected i.c.m. with 2 μL of viral vectors expressing EGFP or mVEGF-C. One month later, T1-weighted MRI acquisition was performed after i.c.m. injection of 5 μL of gadolinium (25 mM in saline). Using the Lymph4D software, it was possible to measure the rate of contrast agent influx into the delineated brain hippocampal region of mice from both groups (scale bar, 3 mm). Images in sequence 2 and subsequent were obtained by subtraction of sequence 1. **r,** Quantification of the signal intensity gain (relative to sequence 1) in the hippocampus revealed a significant increase in the mVEGF-C group, when compared to EGFP (mean ± s.e.m., $n = 4$ per group; repeated measures two-way ANOVA with Bonferroni's post-hoc; data was pooled from 2 independent experiments).

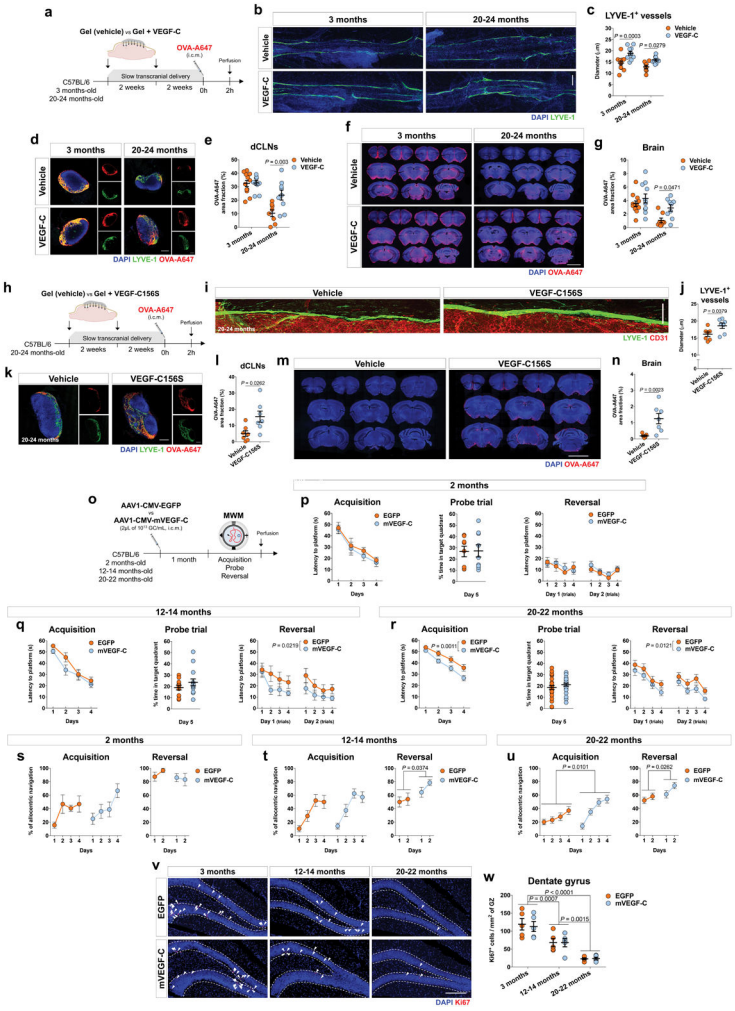

Extended Data Figure 7. Treatment with VEGF-C ameliorates meningeal lymphatic function, brain perfusion by CSF macromolecules and cognitive performance in old mice

a, Hydrogel alone (vehicle) or containing recombinant human VEGF-C (200 ng/mL) was applied on top of a thinned skull surface of adult (3 months-old) and old mice (20–24 months-old). Gels were re-applied two weeks later. Four weeks after the initial treatment, 5 µL of OVA-A647 (in artificial CSF) was injected into the CSF (i.c.m.) and mice were transcardially perfused 2 h later. **b,** Representative images of DAPI (blue) staining and LYVE-1^{+} vessels (in green) in the superior sagittal sinus after transcranial delivery of VEGF-C (scale bar, 50 µm). **c,** Treatment with VEGF-C resulted in significant increase of lymphatic vessel diameter in the superior sagittal sinus in both adult and old mice. **d,** Representative sections of dCLNs stained with DAPI (blue) and for LYVE-1 (green) showing drained OVA-A647 (red; scale bar, 200 µm). **e,** Quantification of OVA-A647 (red) area fraction (%) in the dCLNs showed increased drainage in old mice treated with VEGF-C, when compared to vehicle-treated age-matched mice. **f,** Representative brain sections stained with DAPI (blue) showing OVA-A647 (red) influx into the brain parenchyma (scale bar, 5 mm). **g,** Influx of OVA-A647 into the brain parenchyma of old mice was significantly increased after transcranial delivery of VEGF-C. Data in **c**, **e** and **g** are presented as mean ±

s.e.m., $n = 12$ in vehicle at 3 months, $n = 11$ in VEGF-C at 3 months, $n = 8$ in vehicle at 20–24 months and $n = 9$ in VEGF-C at 20–24 months; two-way ANOVA with Bonferroni's post-hoc test was used in **c**, **e** and **g**; data in **a**–**g** was pooled from 2 independent experiments. **h,** Hydrogel alone (vehicle) or containing recombinant human VEGF-C156S (200 ng/mL) was applied on top of a thinned skull surface of old mice. Gels were re-applied two weeks later. **i,** Whole-mounts of brain meninges were stained for LYVE-1 (green) and CD31 (red). Images show insets of lymphatic vessels near the superior sagittal sinus (scale bar, 100 μm). **j,** Old mice that received VEGF-C156S treatment showed increased diameter of LYVE-1^+ vessels in the superior sagittal sinus. **k,** Representative sections of dCLNs stained with DAPI (blue) and for LYVE-1 (green) showing levels of OVA-A647 (red) drained from the CSF (scale bar, 200 μm). **l,** Quantification of OVA-A647 area fraction (%) in the dCLNs showed a significant increase in VEGF-C156S group when compared to vehicle. **m,** Representative images of OVA-A647 (red) in brain sections also stained with DAPI (blue; scale bar, 5 mm). **n,** Quantification of OVA-A647 area fraction (%) in brain sections showed a significant increase in brain influx of the tracer in old mice treated with VEGF-C156S. Data in **j**, **l** and **n** is presented as mean ± s.e.m., $n = 7$ mice per group; two-tailed Mann-Whitney test was used in **j**, **l** and **n**; data in **h**–**n** was pooled from 2 independent experiments. **o,** Young-adult (2 months), middle-aged (12–14 months) or old (20–22 months) mice were injected with viral vectors expressing EGFP or mVEGF-C. One month after injection, learning and memory was assessed using the MWM test. **p,** Injection of mVEGF-C virus in young-adult mice did not alter their performance in the acquisition, probe trial or reversal of the MWM (mean ± s.e.m., $n = 8$ in EGFP and $n = 9$ in mVEGF-C; repeated measures two-way ANOVA with Bonferroni's post-hoc test was used in the acquisition and reversal; two-tailed Mann-Whitney test was used in the probe trial; data was obtained in a single experiment). **q,** Injection of mVEGF-C virus in middle-aged mice did not alter their performance in the acquisition and in the probe trial, but significantly improved their performance in the reversal (mean ± s.e.m., $n = 12$ in EGFP and $n = 14$ in mVEGF-C; repeated measures two-way ANOVA with Bonferroni's post-hoc test was used in the acquisition and reversal, two-tailed Mann-Whitney test was used in the probe trial; data was pooled from 2 independent experiments). **r,** Injection of mVEGF-C virus in old mice did not alter their performance in the probe trial, but significantly improved their performance in the acquisition and in the reversal (mean ± s.e.m., $n = 25$ in EGFP and $n = 25$ in mVEGF-C; repeated measures two-way ANOVA with Bonferroni's post-hoc test was used in the acquisition and reversal; two-tailed Mann-Whitney test was used in the probe trial; data was pooled from 3 independent experiments). **s–u,** Treatment of (**s**) young-adult mice with mVEGF-C did not affect the % of allocentric navigation strategies used in the MWM. The % of allocentric navigation strategies was significantly higher in (**t**) middle-aged mice treated with mVEGF-C during the reversal and in (**u**) old mice treated with mVEGF-C during the acquisition and reversal, when compared to their age-matched EGFP-treated counterparts. Data in **s**–**u** is presented as mean ± s.e.m.; $n = 8$ in EGFP and $n = 9$ in mVEGF-C at 2 months in **s**; $n = 12$ in EGFP and $n = 14$ in mVEGF-C at 12–14 months in **t**; $n = 25$ per group at 20–22 months in **u**; repeated measures two-way ANOVA with Bonferroni's post-hoc test was used in **s**–**u**; data in **s** was obtained from a single experiment, data in **t** was pooled from 2 independent experiments and data in **u** was pooled from 3 independent experiments. **v,** Insets of the hippocampal dentate gyrus (granular zone, GZ),

stained with DAPI (blue) and for Ki67 (in red), in mice injected with viral vectors expressing EGFP or mVEGF-C at 2, 12–14 and 20–22 months (scale bar, 200 μm). **w,** Aging induced a significant decrease in Ki67$^+$ proliferating cells in the dentate gyrus. Expression of mVEGF-C in the meninges at the analyzed ages did not affect the number of Ki67$^+$ cells in the dentate gyrus (mean ± s.e.m., n = 5 per group; two-way ANOVA with Bonferroni's post-hoc test).

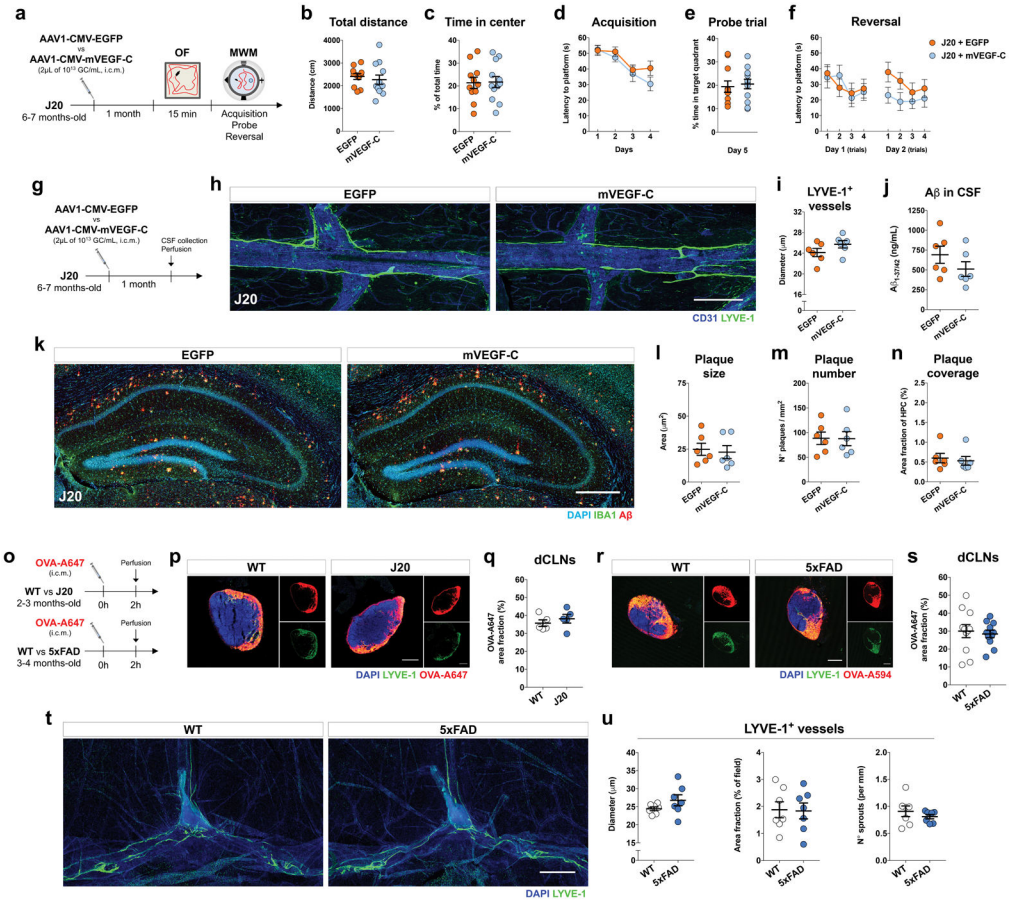

Extended Data Figure 8. Expression of mVEGF-C in the meninges of J20 mice does not ameliorate lymphatic drainage or brain amyloid pathology

a, J20 mice were injected i.c.m. with 2 μL of AAV1-CMV-EGFP or AAV1-CMV-mVEGF-C (10^{13} GC/mL) at 6–7 months. One month after injection, the mice were tested in the open field (OF) and in the MWM. **b, c,** Total distance and % of time in the center of the OF arena was not ameliorated by treatment of J20 mice with mVEGF-C. **d–f,** No statistically significant differences were observed in the (**d**) acquisition, in the (**e**) probe trial or in the (**f**) reversal of the MWM test after 1 month of mVEGF-C. Data in **b**–**f** is presented as mean ± s.e.m., n = 11 in EGFP, n = 12 in mVEGF-C; two-tailed Mann-Whitney test was used in **b**, **c** and **e** and repeated measures two-way ANOVA with Bonferroni's post-hoc test was used in **d** and **f**; data results from a single experiment. **g,** J20 mice were treated with EGFP or mVEGF-C and, 1 month later, CSF, meninges and brain were collected for analysis. **h,** Representative images of DAPI (blue) and LYVE-1$^+$ lymphatic vessels (green) in the

superior sagittal sinus of mice treated with either EGFP or mVEGF-C (scale bar, 500 μm). **i,** AAV1-mediated expression of mVEGF-C did not affect meningeal lymphatic vessel diameter. **j,** Levels of Aβ in the CSF measured by ELISA remained unaltered after mVEGF-C treatment. **k,** Representative images of dorsal hippocampus (scale bar, 500 μm) of J20 mice of EGFP or mVEGF-C groups stained with DAPI (cyan) and for IBA1 (green) and Aβ (red). **l–n,** No changes were observed in amyloid plaque (**l**) size, (**m**) number or (**n**) coverage between the groups. Data in **i**, **j** and **l–n** is presented as mean ± s.e.m., $n = 6$ per group; two-tailed Mann-Whitney test was used in **i**, **j** and **l–n**; data in **g–n** results from a single experiment. **o,** J20 mice (2–3 months-old) and 5xFAD mice (3–4 months-old), and respective age-matched WT littermate controls, were injected with fluorescent OVA-A647 (i.c.m.) in order to measure drainage into the dCLNs. **p,** Representative images of DAPI (blue) and LYVE-1 (green) staining in dCLNs of WT and J20 mice (scale bar, 200 μm) 2 h after injection of OVA-A647 (red). **q,** Quantification of OVA-A647 area fraction (%) in the dCLNs shows equal levels of tracer in mice from both genotypes (mean ± s.e.m., $n = 5$ per group; two-tailed Mann-Whitney test; representative of 2 independent experiments). **r,** Representative images of DAPI (blue) and LYVE-1 (green) staining in dCLNs of WT and 5xFAD mice (scale bar, 200 μm) 2 h after injection of OVA-A594 (red). **s,** Quantification of OVA-A594 area fraction (%) in the dCLNs shows equal levels of tracer in mice from both genotypes (mean ± s.e.m., $n = 11$ per group; two-tailed Mann-Whitney test; data was pooled from 2 independent experiments). **t,** Representative images of DAPI (blue) and LYVE-1 (green) staining in meningeal whole-mounts of WT and 5xFAD mice at 3–4 months (scale bar, 1 mm). **u,** Measurement of LYVE-1^+ vessel diameter, area fraction and number of sprouts (per mm of vessel) showed no differences between genotypes (mean ± s.e.m., $n = 7$ per group; two-tailed Mann-Whitney test; data was pooled from 2 independent experiments).

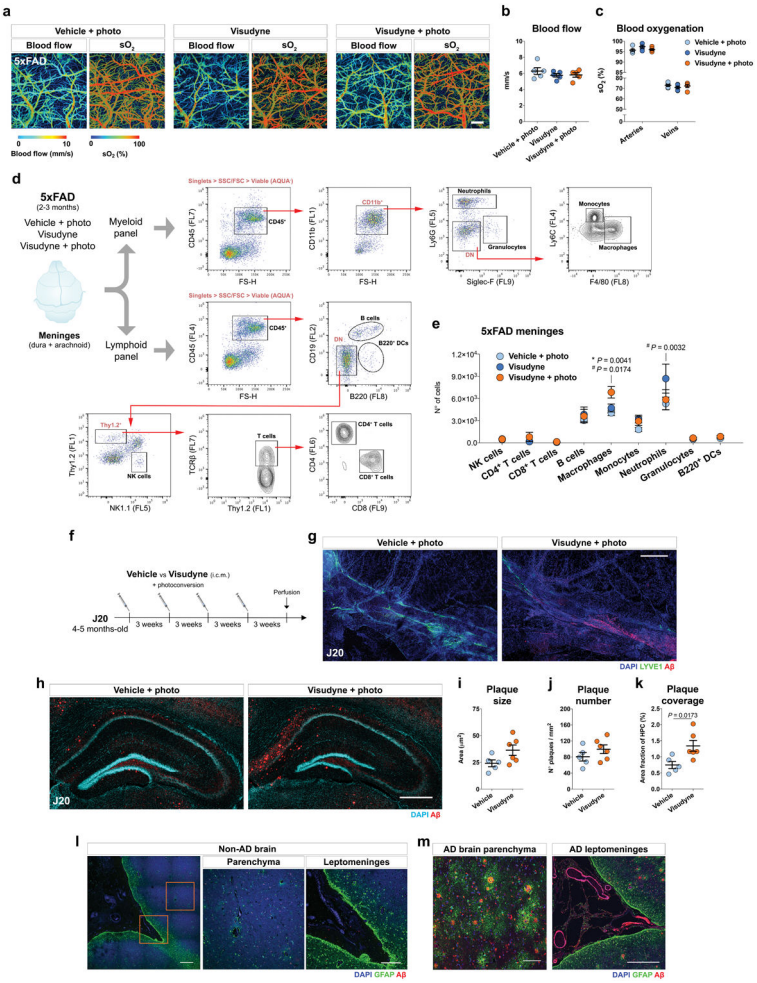

Extended Data Figure 9. Meningeal lymphatic ablation in AD transgenic mice worsens amyloid pathology without affecting blood vessel function

a, Representative images of blood flow (mm/s) and arterial and venous blood oxygenation (% of sO_2) readings obtained by Photoacoustic imaging of brain/meningeal vasculature of 5xFAD mice one week after vehicle/photoconversion, Visudyne or Visudyne/photoconversion. **b, c,** The different treatments did not affect (**b**) blood flow or (**c**) blood oxygenation in the brain/meninges of 5xFAD mice (mean ± s.e.m., $n = 5$ per group; one-way ANOVA with Bonferroni's post-hoc test was used in **b** and two-way ANOVA with Bonferroni's post-hoc test was used in **c**; data results from a single experiment). **d,** Representative flow cytometry dot and contour plots showing the gating strategies used to determine the frequency of specific immune cell populations, using a myeloid or lymphoid panel of markers, in the meninges of 5xFAD after prolonged (1.5 months) meningeal lymphatic ablation. **e,** Analysis of specific immune cell populations in the meninges of 5xFAD mice from the different groups showed a significant increase in macrophages in the Visudyne/photoconversion group when compared to the control groups. A significant increase in neutrophils was observed in Visudyne group, but not in vehicle/photoconversion group, when compared to Visudyne/photoconversion group (mean ± s.e.m., $n = 5$ per group; two-way ANOVA with Holm-Sidak's post-hoc test; *vs vehicle/photoconversion; $^{\#}$vs

Visudyne; data results from a single experiment). **f,** 4–5 months-old J20 mice were submitted to meningeal lymphatic ablation by injection (i.c.m.) of Visudyne or vehicle as a control, followed by a photoconversion step. This procedure was repeated every 3 weeks, for a total of 3 months, to achieve prolonged meningeal lymphatic ablation. **g,** Staining with DAPI (blue) and for LYVE-1 (green) and Aβ (red) in meningeal whole-mounts of J20 mice showing marked amyloid deposition in mice from the Visudyne group (scale bar, 500 μm). **h,** Representative brain sections of J20 mice at 7–8 months stained with DAPI (cyan) and for Aβ (red; scale bar, 500 μm) showing degree of amyloid deposition after meningeal lymphatic ablation. **i–k,** Quantification of amyloid plaque (**i**) size, (**j**) number and (**k**) coverage in the dorsal hippocampus of J20 mice showed a statistically significant increase in coverage in the Visudyne group, when compared to vehicle. Data in **i–k** is presented as mean ± s.e.m., $n = 5$ in vehicle, $n = 6$ in Visudyne; two-tailed Mann-Whitney test was used in **i–k**; experiments in **f–k** were performed once. **l, m,** Sections of human brain cortex, containing meningeal layers (leptomeninges) attached, from (**l**) non-AD brain (scale bar, 500 μm; inset scale bar, 200 μm) and (**m**) AD brain (left image scale bar, 100 μm; right image scale bar, 500 μm) were stained with DAPI (blue), for the astrocyte marker GFAP (green) and for Aβ (red). Data in **l** and **m** results of $n = 8$ non-AD samples and $n = 9$ AD samples and is representative of 2 independent experiments.

Extended data Table 1

Demographic data of AD and Non-AD cases

	Age (years)	Gender	Diagnosis criteria	Pathological score
AD	62	F	Intermediate probability *	A2, B3, C2-3; CAA
	64	M	Possible	CERAD C; BB I/II; CAA
	72	M	High probability *	A3, B3, C3; CAA
	76	F	High probability *	A3, B3, C3; CAA
	79	M	High probability *	A3, B3, C3; CAA
	83	F	High probability *	A3, B3, C3; CAA
	83	M	Intermediate probability *	A2, B2, C2
	88	F	High probability *	A3, B3, C3; CAA
	95	F	Definitive	CERAD C; BB V/VI; CAA
Mean ± SE	78 ± 3.6			
	Age (years)	Gender	Cause of death	
Non-AD	63	F	Multi-organ failure after motor vehicle accident	
	63	M	Acute myocardial infarct	
	64	M	Bilateral pulmonary emboli	
	65	F	Decompensated ischemic cardiomyopathy	
	70	M	Bronchopneumonia	
	73	F	Septicemia	
	80	F	Bronchopneumonia	
	91	F	Cardiovascular atherosclerotic disease	
Mean ± SE	71.1 ± 3.5			

* new criteria for diagnosis following the guidelines of NIA-AA based on ABC (Amyloid, Braak, CERAD) score

AD – Alzheimer's disease; CERAD - Consortium to Establish a Registry for Alzheimer's disease; BB - Braak and Braak stage; CAA – cerebral amyloid angiopathy

Supplementary Material

Refer to Web version on PubMed Central for supplementary material.

Acknowledgments

We thank S. Smith for editing the manuscript, J. Roy for MRI expertise, N. Al-Hamadani for animal care, Guillermo Oliver (Feinberg School of Medicine, Northwestern University, Chicago, USA) for Prox1$^{+/-}$ mice. This work was supported by grants from the National Institutes of Health/National Institute on Aging (AG034113 and AG057496), the Cure Alzheimer's Fund, Owens Family Foundation and the Thomas H. Lowder Family Foundation (awarded to J.K.), the Hobby Foundation (awarded to A.V. and S.T.A.) and American Cancer Society (IRG 81-001-26 awarded to J.M.M.). We thank all the members of the Kipnis Laboratory and the BIG center for their valuable comments during numerous discussions of this work.

References

1. Hasek M, Chutna J, Sladecek M, Lodin Z. Immunological tolerance and tumor allografts in the brain. Nature. 1977; 268:68–69. [PubMed: 887149]
2. Louveau A, Harris TH, Kipnis J. Revisiting the Mechanisms of CNS Immune Privilege. Trends Immunol. 2015; 36:569–577. [PubMed: 26431936]
3. Kipnis J. Multifaceted interactions between adaptive immunity and the central nervous system. Science. 2016; 353:766–771. [PubMed: 27540163]
4. Louveau A, et al. Structural and functional features of central nervous system lymphatic vessels. Nature. 2015; 523:337–341. [PubMed: 26030524]
5. Aspelund A, et al. A dural lymphatic vascular system that drains brain interstitial fluid and macromolecules. J Exp Med. 2015; 212:991–999. [PubMed: 26077718]
6. Absinta M, et al. Human and nonhuman primate meninges harbor lymphatic vessels that can be visualized noninvasively by MRI. Elife. 2017; 6
7. Deane R, et al. apoE isoform-specific disruption of amyloid beta peptide clearance from mouse brain. J Clin Invest. 2008; 118:4002–4013. [PubMed: 19033669]
8. Zhao Z, et al. Central role for PICALM in amyloid-beta blood-brain barrier transcytosis and clearance. Nat Neurosci. 2015; 18:978–987. [PubMed: 26005850]
9. Deane R, et al. RAGE mediates amyloid-beta peptide transport across the blood-brain barrier and accumulation in brain. Nat Med. 2003; 9:907–913. [PubMed: 12808450]
10. Mildner A, et al. Distinct and non-redundant roles of microglia and myeloid subsets in mouse models of Alzheimer's disease. J Neurosci. 2011; 31:11159–11171. [PubMed: 21813677]
11. Keren-Shaul H, et al. A Unique Microglia Type Associated with Restricting Development of Alzheimer's Disease. Cell. 2017; 169:1276–1290. e1217. [PubMed: 28602351]
12. Iliff JJ, et al. A paravascular pathway facilitates CSF flow through the brain parenchyma and the clearance of interstitial solutes, including amyloid beta. Sci Transl Med. 2012; 4:147ra111.
13. Kress BT, et al. Impairment of paravascular clearance pathways in the aging brain. Ann Neurol. 2014; 76:845–861. [PubMed: 25204284]
14. Peng W, et al. Suppression of glymphatic fluid transport in a mouse model of Alzheimer's disease. Neurobiol Dis. 2016; 93:215–225. [PubMed: 27234656]
15. Brookmeyer R, Abdalla N, Kawas CH, Corrada MM. Forecasting the prevalence of preclinical and clinical Alzheimer's disease in the United States. Alzheimers Dement. 2018; 14:121–129. [PubMed: 29233480]
16. Erkkinen MG, Kim MO, Geschwind MD. Clinical Neurology and Epidemiology of the Major Neurodegenerative Diseases. Cold Spring Harb Perspect Biol. 2018; 10
17. Benilova I, Karran E, De Strooper B. The toxic Abeta oligomer and Alzheimer's disease: an emperor in need of clothes. Nat Neurosci. 2012; 15:349–357. [PubMed: 22286176]

18. Joachim CL, Duffy LK, Morris JH, Selkoe DJ. Protein chemical and immunocytochemical studies of meningovascular beta-amyloid protein in Alzheimer's disease and normal aging. Brain Res. 1988; 474:100–111. [PubMed: 3214703]
19. Xu Z, et al. Deletion of aquaporin-4 in APP/PS1 mice exacerbates brain Abeta accumulation and memory deficits. Mol Neurodegener. 2015; 10:58. [PubMed: 26526066]
20. Chevalier S, Ferland G, Tuchweber B. Lymphatic absorption of retinol in young, mature, and old rats: influence of dietary restriction. FASEB J. 1996; 10:1085–1090. [PubMed: 8801171]
21. Hos D, Bachmann B, Bock F, Onderka J, Cursiefen C. Age-related changes in murine limbal lymphatic vessels and corneal lymphangiogenesis. Exp Eye Res. 2008; 87:427–432. [PubMed: 18755186]
22. Nagai T, Bridenbaugh EA, Gashev AA. Aging-associated alterations in contractility of rat mesenteric lymphatic vessels. Microcirculation. 2011; 18:463–473. [PubMed: 21466607]
23. Tammela T, et al. Photodynamic ablation of lymphatic vessels and intralymphatic cancer cells prevents metastasis. Sci Transl Med. 2011; 3:69ra11.
24. Kilarski WW, et al. Optimization and regeneration kinetics of lymphatic-specific photodynamic therapy in the mouse dermis. Angiogenesis. 2014; 17:347–357. [PubMed: 23892627]
25. Escobedo N, et al. Restoration of lymphatic function rescues obesity in Prox1-haploinsufficient mice. JCI Insight. 2016; 1
26. Ringstad G, Vatnehol SAS, Eide PK. Glymphatic MRI in idiopathic normal pressure hydrocephalus. Brain. 2017
27. Zeppenfeld DM, et al. Association of Perivascular Localization of Aquaporin-4 With Cognition and Alzheimer Disease in Aging Brains. JAMA Neurol. 2017; 74:91–99. [PubMed: 27893874]
28. Rudy JW, Huff NC, Matus-Amat P. Understanding contextual fear conditioning: insights from a two-process model. Neurosci Biobehav Rev. 2004; 28:675–685. [PubMed: 15555677]
29. Owen SF, et al. Oxytocin enhances hippocampal spike transmission by modulating fast-spiking interneurons. Nature. 2013; 500:458–462. [PubMed: 23913275]
30. Zhang G, et al. Hypothalamic programming of systemic ageing involving IKK-beta, NF-kappaB and GnRH. Nature. 2013; 497:211–216. [PubMed: 23636330]
31. Liebl J, et al. Cdk5 controls lymphatic vessel development and function by phosphorylation of Foxc2. Nat Commun. 2015; 6:7274. [PubMed: 26027726]
32. Jeltsch M, et al. CCBE1 enhances lymphangiogenesis via A disintegrin and metalloprotease with thrombospondin motifs-3-mediated vascular endothelial growth factor-C activation. Circulation. 2014; 129:1962–1971. [PubMed: 24552833]
33. Shin JW, et al. Prox1 promotes lineage-specific expression of fibroblast growth factor (FGF) receptor-3 in lymphatic endothelium: a role for FGF signaling in lymphangiogenesis. Mol Biol Cell. 2006; 17:576–584. [PubMed: 16291864]
34. Saaristo A, et al. Lymphangiogenic gene therapy with minimal blood vascular side effects. J Exp Med. 2002; 196:719–730. [PubMed: 12235206]
35. Karkkainen MJ, et al. A model for gene therapy of human hereditary lymphedema. Proc Natl Acad Sci U S A. 2001; 98:12677–12682. [PubMed: 11592985]
36. Joukov V, et al. A recombinant mutant vascular endothelial growth factor-C that has lost vascular endothelial growth factor receptor-2 binding, activation, and vascular permeability activities. J Biol Chem. 1998; 273:6599–6602. [PubMed: 9506953]
37. Han J, et al. Vascular endothelial growth factor receptor 3 controls neural stem cell activation in mice and humans. Cell Rep. 2015; 10:1158–1172. [PubMed: 25704818]
38. Meshi D, et al. Hippocampal neurogenesis is not required for behavioral effects of environmental enrichment. Nat Neurosci. 2006; 9:729–731. [PubMed: 16648847]
39. Harris JA, et al. Many neuronal and behavioral impairments in transgenic mouse models of Alzheimer's disease are independent of caspase cleavage of the amyloid precursor protein. J Neurosci. 2010; 30:372–381. [PubMed: 20053918]
40. Palop JJ, et al. Aberrant excitatory neuronal activity and compensatory remodeling of inhibitory hippocampal circuits in mouse models of Alzheimer's disease. Neuron. 2007; 55:697–711. [PubMed: 17785178]

41. Oakley H, et al. Intraneuronal beta-amyloid aggregates, neurodegeneration, and neuron loss in transgenic mice with five familial Alzheimer's disease mutations: potential factors in amyloid plaque formation. J Neurosci. 2006; 26:10129–10140. [PubMed: 17021169]
42. Sagare AP, et al. Pericyte loss influences Alzheimer-like neurodegeneration in mice. Nat Commun. 2013; 4:2932. [PubMed: 24336108]
43. Sevigny J, et al. Addendum: The antibody aducanumab reduces Abeta plaques in Alzheimer's disease. Nature. 2017; 546:564. [PubMed: 28640269]
44. Mucke L, et al. High-level neuronal expression of abeta 1–42 in wild-type human amyloid protein precursor transgenic mice: synaptotoxicity without plaque formation. J Neurosci. 2000; 20:4050–4058. [PubMed: 10818140]
45. Richard BC, et al. Gene Dosage Dependent Aggravation of the Neurological Phenotype in the 5XFAD Mouse Model of Alzheimer's Disease. J Alzheimers Dis. 2015; 45:1223–1236. [PubMed: 25697701]
46. Harvey NL, et al. Lymphatic vascular defects promoted by Prox1 haploinsufficiency cause adult-onset obesity. Nat Genet. 2005; 37:1072–1081. [PubMed: 16170315]
47. Cirrito JR, et al. In vivo assessment of brain interstitial fluid with microdialysis reveals plaque-associated changes in amyloid-beta metabolism and half-life. J Neurosci. 2003; 23:8844–8853. [PubMed: 14523085]
48. Hinder LM, Vincent AM, Hayes JM, McLean LL, Feldman EL. Apolipoprotein E knockout as the basis for mouse models of dyslipidemia-induced neuropathy. Exp Neurol. 2013; 239:102–110. [PubMed: 23059459]
49. Caicco MJ, et al. A hydrogel composite system for sustained epi-cortical delivery of Cyclosporin A to the brain for treatment of stroke. J Control Release. 2013; 166:197–202. [PubMed: 23306024]
50. Ning B, et al. Ultrasound-aided Multi-parametric Photoacoustic Microscopy of the Mouse Brain. Sci Rep. 2015; 5:18775. [PubMed: 26688368]
51. Derecki NC, et al. Wild-type microglia arrest pathology in a mouse model of Rett syndrome. Nature. 2012; 484:105–109. [PubMed: 22425995]
52. Louveau A, et al. Impaired spatial memory in mice lacking CD3zeta is associated with altered NMDA and AMPA receptors signaling independent of T-cell deficiency. J Neurosci. 2013; 33:18672–18685. [PubMed: 24259588]
53. Derecki NC, et al. Regulation of learning and memory by meningeal immunity: a key role for IL-4. J Exp Med. 2010; 207:1067–1080. [PubMed: 20439540]
54. Janus C. Search strategies used by APP transgenic mice during navigation in the Morris water maze. Learn Mem. 2004; 11:337–346. [PubMed: 15169864]
55. Garthe A, Kempermann G. An old test for new neurons: refining the Morris water maze to study the functional relevance of adult hippocampal neurogenesis. Front Neurosci. 2013; 7:63. [PubMed: 23653589]
56. Montine TJ, et al. National Institute on Aging-Alzheimer's Association guidelines for the neuropathologic assessment of Alzheimer's disease: a practical approach. Acta Neuropathol. 2012; 123:1–11. [PubMed: 22101365]
57. Andrews S. FastQC: a quality control tool for high throughput sequence data. 2010
58. Harrow J, et al. GENCODE: the reference human genome annotation for The ENCODE Project. Genome Res. 2012; 22:1760–1774. [PubMed: 22955987]
59. Patro R, Duggal G, Love MI, Irizarry RA, Kingsford C. Salmon provides fast and bias-aware quantification of transcript expression. Nat Methods. 2017; 14:417–419. [PubMed: 28263959]
60. Soneson C, Love MI, Robinson MD. Differential analyses for RNA-seq: transcript-level estimates improve gene-level inferences. F1000Res. 2015; 4:1521. [PubMed: 26925227]
61. Love MI, Huber W, Anders S. Moderated estimation of fold change and dispersion for RNA-seq data with DESeq2. Genome Biol. 2014; 15:550. [PubMed: 25516281]
62. Leek JT, Storey JD. Capturing heterogeneity in gene expression studies by surrogate variable analysis. PLoS Genet. 2007; 3:1724–1735. [PubMed: 17907809]

63. Leek JT, Johnson WE, Parker HS, Jaffe AE, Storey JD. The sva package for removing batch effects and other unwanted variation in high-throughput experiments. Bioinformatics. 2012; 28:882–883. [PubMed: 22257669]

64. Yu G, Wang LG, Han Y, He QY. clusterProfiler: an R package for comparing biological themes among gene clusters. OMICS. 2012; 16:284–287. [PubMed: 22455463]

65. Kolde R. Pheatmap: pretty heatmaps. R package version. 2012; 61

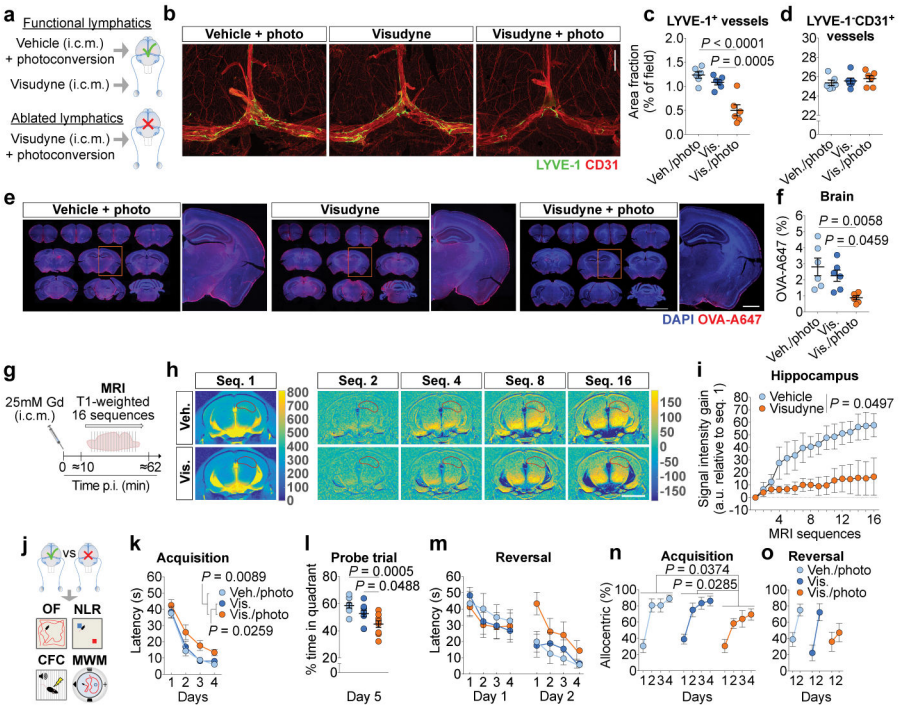

Figure 1. Impairing meningeal lymphatics affects brain CSF influx and ISF diffusion and worsens cognitive function

a, Seven days after lymphatic ablation mice were injected with 5 μL of ovalbumin-Alexa647 (OVA-A647) into the cisterna magna (i.c.m.). **b,** Representative images of meningeal whole-mounts stained for LYVE-1/CD31 (scale bar, 1 mm). **c, d,** Quantification of area fraction (%) occupied by (**c**) LYVE-1^{+} lymphatic vessels and (**d**) LYVE-1^{-}CD31^{+} blood vessels. **e,** Representative brain sections showing 4′,6-diamidino-2-phenylindole (DAPI) and OVA-A647 (scale bar, 5 mm; inset scale bar, 1 mm). **f,** Quantification of OVA-A647 area fraction. Data in **c**, **d** and **f** is presented as mean ± s.e.m., $n = 6$ per group; one-way ANOVA with Bonferroni's post-hoc test was used in **c**, **d** and **f; a**–**f** is representative of 2 independent experiments; significant differences between vehicle/photoconversion and Visudyne/photoconversion were replicated in 5 independent experiments. **g,** Gadolinium (Gd) was injected (i.c.m.) and T1-weighted magnetic resonance imaging (MRI) acquisition was performed 7 days after meningeal lymphatic ablation. **h,** Representative images of sequence 1 and of Gd intensity gain in subsequent sequences (hippocampus delineated in red; scale bar, 3 mm). **i,** Quantification of the Gd signal intensity gain over 16 sequences (relative to sequence 1) in hippocampus. Data in **i** is presented as mean ± s.e.m., $n = 4$ per group; repeated measures two-way ANOVA with Bonferroni's post-hoc test; **g**–**i** is representative of 2 independent experiments. **j,** Meningeal lymphatic ablation was performed twice and two weeks after the last intervention, open field (OF), novel location recognition (NLR), contextual fear conditioning (CFC) and Morris water maze (MWM) behavioral tests were performed (Extended data Fig. 5 for OF, NLR and CFC). **k,** Latency to platform (acquisition). **l,** Time spent (%) in the target quadrant (probe). **m,** Latency to platform (reversal). **n, o,** Allocentric navigation strategies (%) used in the MWM (**n**) acquisition and (**o**) reversal. Data in **k**–**m** and **n**, **o** are presented as mean ± s.e.m., $n = 9$ per group; repeated

measures two-way ANOVA with Bonferroni's post-hoc test was used in **k**, **m**, **n** and **o**; one-way ANOVA with Bonferroni's post-hoc test was used in **l**; significant differences between vehicle/photoconversion and Visudyne/photoconversion were replicated in 3 independent experiments.

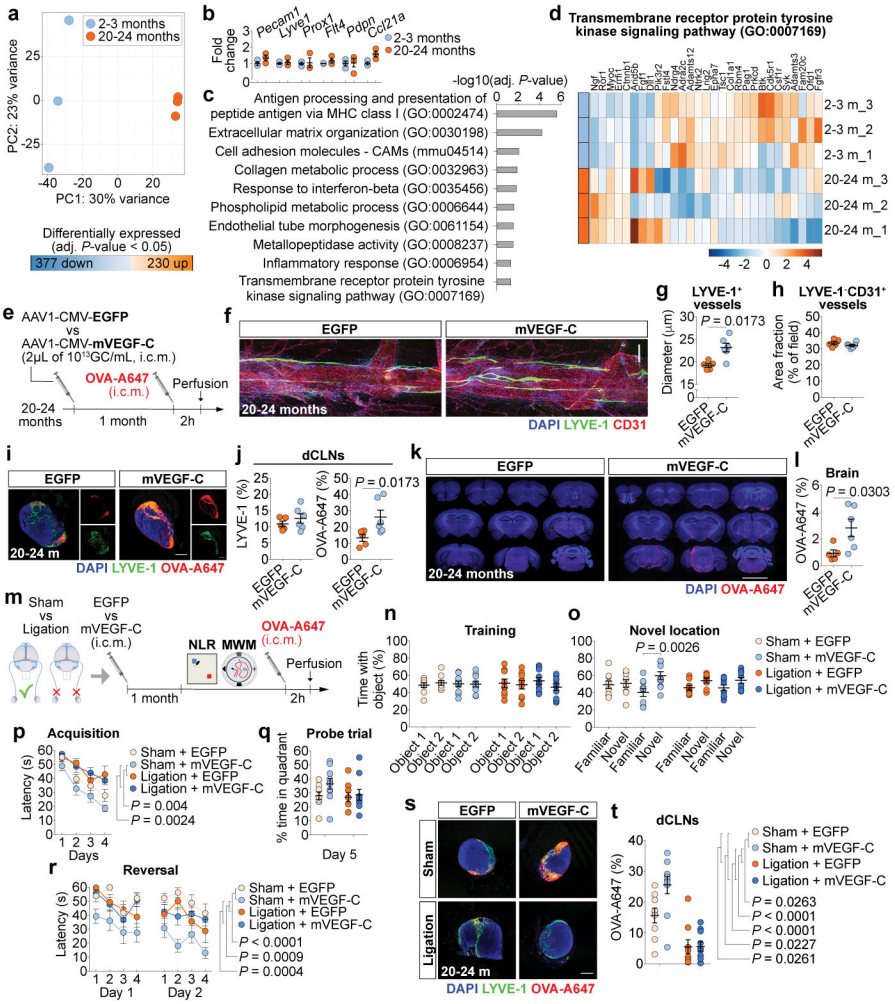

Figure 2. Improving meningeal lymphatic function in aged mice increases brain perfusion and alleviates cognitive deficits

a, Principal component (PC) analysis plot for RNA-seq of lymphatic endothelial cells (LECs) from meninges of young-adult and aged mice. 230 genes up- and 377 genes down-regulated in meningeal LECs at 20–24 months. **b,** Expression of *Pecam1*, *Lyve1*, *Prox1*, *Flt4*, *Pdpn* and *Ccl21a*. **c,** Gene sets obtained by functional enrichment of differentially expressed genes in meningeal LECs at 20–24 months. **d,** Heatmap showing relative expression level of genes involved in Transmembrane receptor protein tyrosine kinase signaling pathway (color scale bar values represent standardized rlog-transformed values across samples). Data in **a–d** consists of $n = 3$ per group (individual RNA samples result from LECs pooled from 10 meninges over 2 independent experiments); data in **b** is presented as mean ± s.e.m. with two-way ANOVA with Bonferroni's post-hoc test; in **a–c** *P*-values were corrected for multiple hypothesis testing with the Benjamini–Hochberg false discovery rate procedure; in **c** and **d** functional enrichment of differential expressed genes performed using gene sets from GO and KEGG and determined with Fisher's exact test. **e,** Old mice were injected (i.c.m.) with 2 µL of AAV1-CMV-EGFP (EGFP) or AAV1-CMV-mVEGF-C (mVEGF-C), at 10^{13} genome copies (GC)/mL. One month later, OVA-A647 was

injected i.c.m. **f,** Insets of the superior sagittal sinus showing DAPI/LYVE-1/CD31 (scale bar, 200 μm). **g, h,** Quantification of (**g**) diameter of LYVE-1^+ lymphatic vessels and of (**h**) area fraction (%) of LYVE-1^-CD31^+ blood vessels. **i,** Representative sections of deep cervical lymph nodes (dCLNs) showing DAPI/LYVE-1/OVA-A647 (scale bar, 200 μm). **j,** Quantification of LYVE-1 and OVA-A647 area fraction in dCLNs. **k,** Representative brain coronal sections showing DAPI/OVA-A647 (scale bar, 5 mm). **l,** Quantification of OVA-A647 area fraction in brain sections. Data in **g**, **h**, **j** and **l** are presented as mean ± s.e.m., n = 5 in EGFP, n = 6 in mVEGF-C; two-tailed Mann-Whitney test was used in **g**, **h**, **j** and **l; e**–**l** is representative of 2 independent experiments. **m,** Old mice were injected with EGFP or mVEGF-C viruses (i.c.m.) after ligation of the lymphatics afferent to the dCLNs or sham surgery. One month later, learning and memory was assessed in the NLR and MWM tests and mice were injected (i.c.m.) with OVA-A647. **n, o,** Time with the object (%) was assessed in the NLR (**n**) training and (**o**) novel location tasks. **p,** Latency to platform (acquisition). **q,** Time spent (%) in the target quadrant (probe). **r,** Latency to platform (reversal). **s,** Representative sections of dCLNs showing DAPI/LYVE-1/OVA-A647 (scale bar, 200 μm). **t,** Quantification of OVA-A647 area fraction in dCLNs. Data in **n**–**r** and **t** is presented as mean ± s.e.m., n = 9 in sham + EGFP and ligation + EGFP, n = 10 in sham + mVEGF-C and ligation + mVEGF-C; two-way ANOVA with Bonferroni's post-hoc test was used in **n**, **o**, **q** and **t**; repeated measures two-way ANOVA with Bonferroni's post-hoc test was used in **p** and **r; m**–**t** results from 2 independent experiments.

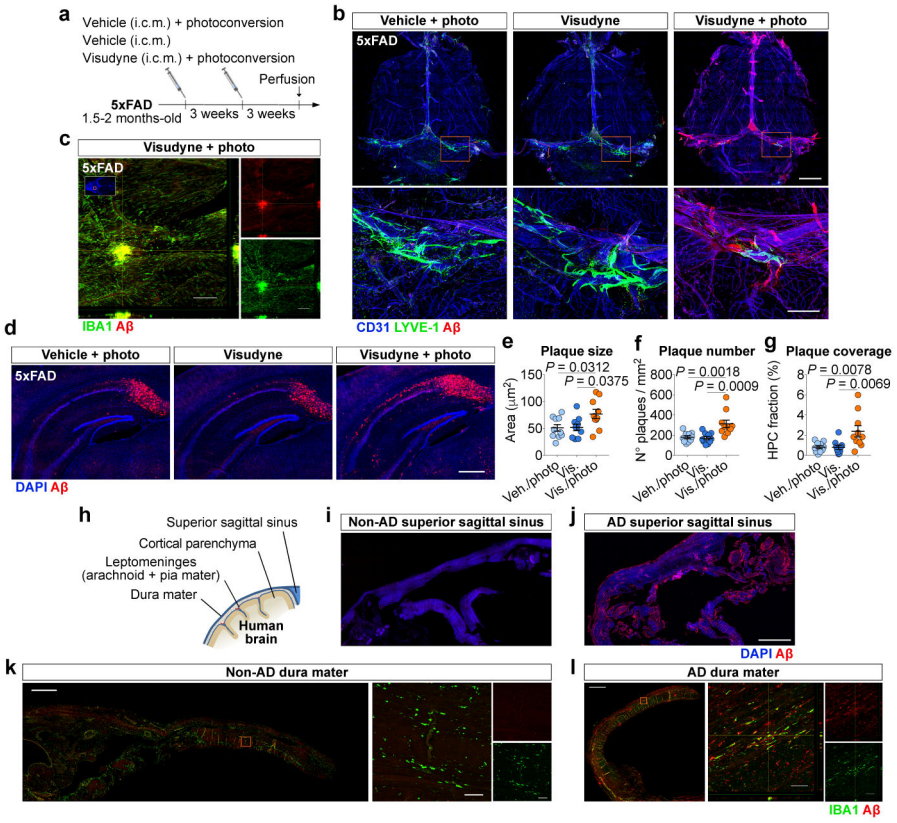

Figure 3. Ablation of meningeal lymphatics aggravates amyloid pathology in AD transgenic mice

a, Young-adult 5xFAD mice were submitted to meningeal lymphatic ablation or control procedures. Procedures were repeated 3 weeks later and amyloid pathology was assessed 6 weeks after initial treatment. **b,** Staining for CD31/LYVE-1/Aβ in meninges (scale bar, 2 mm; inset scale bar, 500 μm). **c,** Orthogonal view of IBA^+ macrophages clustering around an amyloid plaque in meninges of a 5xFAD with ablated lymphatics (scale bar, 200 μm). **d,** Representative images of DAPI/Aβ in the hippocampus of 5xFAD mice from each group (scale bar, 500 μm). **e–g,** Quantification of amyloid plaque (**e**) size, (**f**) number and (**g**) coverage in the hippocampus of 5xFAD mice. Data in **e–g** is presented as mean ± s.e.m., n = 10 per group; one-way ANOVA with Bonferroni's post-hoc test was used in **e–g; a–g** is representative of 2 independent experiments. **h,** Staining for amyloid pathology was performed in human non-AD and AD brains (Extended data Fig. 9) and different meningeal layers. **i, j,** Meningeal superior sagittal sinus tissue of (**i**) non-AD or (**j**) AD patients stained with DAPI/Aβ (scale bar, 2 mm). **k, l,** Meningeal dura mater tissue of (**k**) non-AD or (**l**) AD patients, stained for IBA1/Aβ (scale bars, 1 mm; orthogonal view inset scale bars, 50 μm). Data in **h–l** results of n = 8 non-AD samples and n = 9 AD samples and is representative of 2 independent experiments.